Alma Mater Studiorum · Università di Bologna

Scuola di Scienze

Dipartimento di Fisica e Astronomia - DIFA

Corso di Laurea Magistrale in Fisica

Ultrafast Electron Diffraction on Materials Exposed to Intense Free Electron Laser Pulses

Tesi di Laurea Magistrale
in
Materials Physics and Nanoscience

Relatore:
Prof. Federico Boscherini

Presentata da:
Giorgio Cortelli

Correlatore:
Dott. Emiliano Principi

Anno Accademico 2018/2019

Abstract

The advent of Free Electron Lasers (FELs) has opened unprecedented opportunities for the study of transient states of matter. The use of the seeding technique, developed at the FERMI FEL in Trieste (Italy), pushed further the frontier allowing to perform pump-probe experiments with femtosecond time resolution. FELs permit shedding light onto unexplored non-equilibrium dynamics and processes in matter. In this thesis, a pioneering setup for monitoring sub-picosecond atomic structure changes in materials is described. The FEL is used as an isochoric pump while a 100 keV compressed electron bunch is used as a structural probe thus obtaining an ultrafast electron diffraction (UED) facility. Results of a pilot UED experiment on selected samples (gold and diamond) are presented and analyzed.

Keywords: Free Electron Laser, Ultrafast Electron Diffraction, ultrafast melting

Abstract (italiano)

L'avvento dei Free Electron Lasers (FELs) ha aperto opportunità senza precedenti per lo studio degli stati transitori della materia. FERMI FEL a Trieste (Italia), ha spinto oltre la frontiera per eseguire esperimenti pump-probe con risoluzione temporale dell'ordine del femtosecondo. I FEL consentono di far luce su dinamiche e processi di non-equilibrio inesplorati nella materia. In questa tesi è descritta una configurazione pionieristica per il monitoraggio dei cambiamenti della struttura atomica dei materiali in scale di tempo inferiori al picosecondo. Il FEL viene utilizzato come pompa isocora mentre a 100 keV un gruppo di elettroni compressi viene utilizzato come sonda ottenendo così uno strumento di diffrazione elettronica ultraveloce (UED). I risultati di un esperimento UED pilota su campioni selezionati (oro e diamante) sono presentati e analizzati.

Keywords: Free Electron Laser, Diffrazione di elettroni risolta in tempo, fusione ultraveloce

Contents

Acronyms

DNA Deoxyribonucleic acid. 3

EUV Extreme Ultraviolet. 1, 4, 14, 16, 24, 26, 27, 38, 39, 46, 50, 51, 61, 73

FEL Free Electron Laser. 1, 3, 4, 10, 14, 16–18, 20, 26, 27, 34, 38–41, 45–48, 50, 52, 61, 73

FWHM Full Width at Half Maximum. 55–57

IR Infrared. 14

LINAC Linear Accelerator. 17, 18, 46

PADReS Photon Analysis Delivery and Reduction System. 19, 40

PEEK PolyEtherEtherKeton. 37

RF Radio Frequency. 17, 34–39, 46, 47, 52, 72, 73

SLU Seed Laser User. 38, 39, 46

TTM Two Temperatures Model. 26

UED Ultrafast Electron Diffraction. 26, 33, 35, 39, 41

UEM Ultrafast Electron Microscopy. 33

Chapter I

Introduction

NOWADAYS one of the major task of the research in condensed matter is the understanding of the ultrafast phenomena taking place in the sub-ps time scale. Ultrafast processes are common to a variety of transient states spanning from the physics, the chemistry and the biochemistry. Processes on those research fields have in common the engagement of electrons, atoms as well as molecules which are the building blocks of matter. Ultrafast melting, photo induced chemical reactions, nanoscale electronic and magnetic reactions are just few examples of the processes happening in the sub-ps time scale when complex systems are driven out of equilibrium. To exemplify, it is interesting to look at the dynamics of the chemical bonding, which is determined by the time evolution of the electron density. Ultrafast pump-probe experimental methods pave the way to the study of ultrafast dynamics in matter. [1] Specific photon energy and pulse duration have to be used to perform such kind of experiments: a sub-ps time resolution is demanded to see atoms, which move over distances of the order of 0.1 nm with speed of few km per second. Ultrafast pump-probe experiments have to be conducted with two different pulses: the pump is used to define a reference time and to trigger the dynamics under investigation, the probe pulse instead, interacting with the sample after a time interval Δt, is sensitive to the evolution of the property of the system. The definition of Δt value requires a jitter smaller than the characteristic times of the investigated dinamics. In order to reach high energy density regimes, the pump must carry enough photons per pulse. In this work we propose a new experimental setup to carry ultrafast pump-probe experiments through the FERMI Free Electron Laser (FEL) as pump and sub-relativistic compressed electron bunches as probe. Chapter II will introduce the equations which govern the FEL emission and how this scheme is modified and implemented into the first seeded FEL facility: FERMI. Chapter III will describe the theoretical reasons why an Extreme Ultraviolet (EUV) pump is suitable for isochoric heating in matter. In Chapter IV the

experimental setup is described. Chapter V presents the unprecedented experimental data obtained with this setup investigating on polycrystalline gold, diamond single crystal and gold single crystal.

Chapter II

Free Electron Lasers

X-RAYS were discovered by Wilhelm Conrad Rontgen in 1895. Since that time, they have become established as an invaluable probe of the structure of matter. The range of materials for which X-rays have proved to be decisive in unraveling the structure is truly staggering. These include at one limit of complexity simple compounds, through to more complex and celebrated examples, such Deoxyribonucleic acid (DNA). In more recent times the structure of proteins, and even functional units of living organisms, can be solved on a regular basis. Progress in both our theoretical understanding of the interaction of X-rays with matter, and in our knowledge of how to exploit them experimentally, was steady from the period covering their discovery through to the mid-1970s. The main limitation in this period was the source, which had remained essentially unchanged from about 1912. In the 1960s it was realized that the synchrotron radiation emitted from electrons circulating in storage rings constructed for nuclear physics experiments was potentially a much more intense and versatile source of X-rays. Indeed, synchrotrons have proven to be such vastly better sources that many storage rings have been constructed around the world dedicated solely to the production of X-rays. This has culminated to date in the so-called third-generation synchrotron sources, which are more brilliant than the early lab-based sources by a factor of approximately 10^{12}, as indicated in Figure II.1.

For decades, scientists have been employing this synchrotron effect to produce high-intensity radiation in a wide spectral range from the far infrared to hard X-rays for research purposes. Modern synchrotron radiation sources do not use single magnets to generate the light, but a series of tens (or even hundreds) of magnets with alternating field, called undulator, in which the electron beam wiggles ("undulates") only slightly about a straight line. In each curve, the electrons generate light which overlaps and interferes constructively for certain wavelengths leading to nearly monochromatic light emitted in a narrow cone. The FEL makes use of the physics of the undulator. The advent of FELs

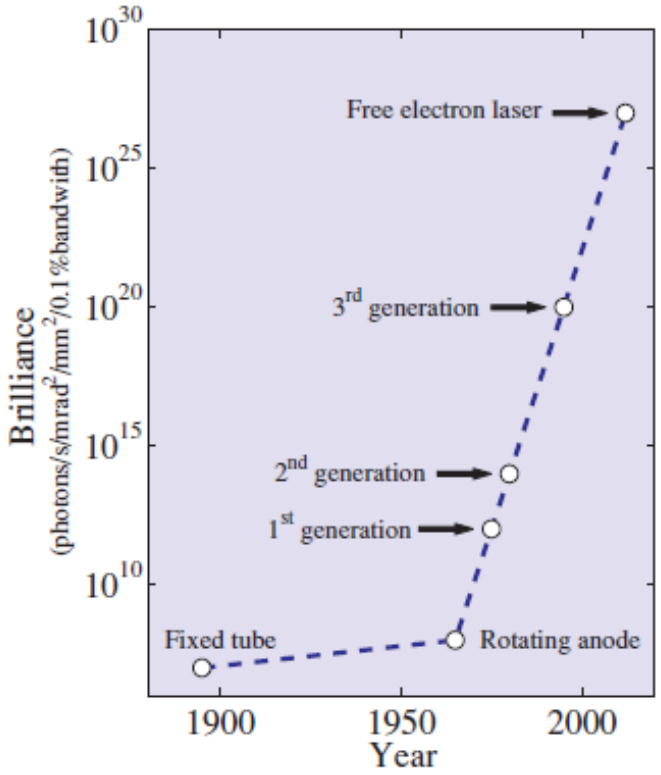

Figure II.1: The brilliance of X-ray sources as a function of time. [2]

opened unprecedented opportunities for the study of condensed matter. The use of the seeding technique, developed at the FERMI FEL in Trieste (Italy), pushed further the frontier allowing to perform pump-probe experiments with femtosecond time resolution. FELs permit shedding light onto unexplored non-equilibrium dynamics and processes in matter. In this chapter, the description of free electron laser radiation emission is reported. In particular, the generation process of a seeded FEL will be introduced and the first seeded FEL, FERMI, operative in the EUV spectral region is described.

1 Electromagnetic Radiation

X-rays are electromagnetic waves with wavelengths spacing in the region of an Å ($\lambda \sim 10^{-10}$). In many cases one is interested in a monochromatic beam of X-rays as shown in Figure II.2. Usually the direction of the beam is taken to be along the z-axis, perpendicular to the electric $\vec{E}$ and magnetic $\vec{B}$ fields. For simplicity the space time dependence only of the electric field is described. Consider now an electromagnetic wave propagating in a three-dimensional space. Assuming that it is monochromatic, we can introduce the wave

vector which is

$$\vec{k} = \frac{2\pi}{\lambda}\hat{k} \tag{II.1}$$

where $\hat{k}$ is the unit vector of the propagation direction of the wave. Mathematically the electric field can be expressed as a sine wave in the complex form $E_0 e^{ikz}$. The spatial and temporal variation of the plane wave propagating along the z-axis can be expressed as

$$\vec{E}(\vec{r}, t) = \hat{\epsilon} E_0 e^{i(\vec{k}\cdot\vec{r} - \omega t)} \tag{II.2}$$

where $\hat{\epsilon}$ is the versor of the propagation of the electric field.

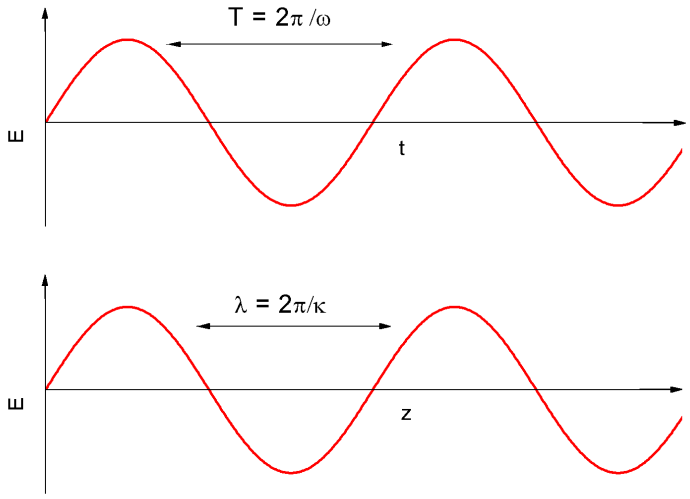

Figure II.2: Electromagnetic wave in space and time domains.

2 Synchrotron Radiation

Synchrotron radiation takes its name from a specific type of electron accelerator. However, synchrotron radiation has become a generic term to describe radiation from charged particles travelling at relativistic speeds in applied magnetic fields which force them to travel along curved paths. Synchrotron radiation is produced in storage rings where electrons or positrons are kept circulating at constant energy. In a storage ring synchrotron radiation is produced either in the bending magnets needed to keep the electrons in a closed orbit, or in insertion devices such as wigglers or undulators situated in the straight sections of the storage ring. In these devices an alternating magnetic field forces the

electrons to follow oscillating paths rather than moving in a straight line. In a wiggler the amplitude of the oscillations is rather large, and the radiation from different wiggles adds incoherently, whereas in undulators, as we shall see, the small-amplitude oscillations of electron bunches produce a coherent addition of the radiation from each oscillation. [2] Consider the radiation emitted by an electron moving in a constant magnetic field. The effect of the field is to accelerate the electron and bend its trajectory into a circular orbit, producing so-called bending magnet radiation in the process. While this type of radiation is not the most brilliant, it nonetheless has many useful properties that are widely exploited in synchrotron research. A non-relativistic electron of momentum $\vec{p} = m\vec{v}$ moving in a constant magnetic field $\vec{B}$ experiences the Lorentz force $\vec{F} = d\vec{p}/dt = -e\vec{v} \times \vec{B}$. In response to this force the electron accelerates and moves in a circular orbit in a plane perpendicular to B. With the two equations it is possible to obtain the relation between the momentum of the particle and the magnetic field

$$\vec{p} = \rho e\vec{B} \tag{II.3}$$

This relation is also valid for relativistic particles, in which case $\vec{p}$ is equal to $\gamma m\vec{B}$, where $\gamma = \frac{Ee}{mc^2}$, the electron energy in units of the rest mass energy. For the case of ultra-relativistic particles $v \cong c$, which pertains to synchrotrons, we have

$$\gamma mc = \rho e\vec{B} \tag{II.4}$$

so that in practical units the radius of an electron orbiting in a synchrotron is given by

$$\rho[m] = \frac{3.3Ee[GeV]}{B[T]} \tag{II.5}$$

The electric field radiated from an accelerating charge is directly proportional to the acceleration. Hence, an electron moving in a circular arc experiences a constant acceleration and radiates continuously throughout its entire orbit. However, the radiation from a relativistic electron moving in a circular orbit is compressed into tightly collimated cones of radiation, as indicated schematically in Figure II.3.

The radiation from an electron orbiting at relativistic speeds in a circular orbit can thus be likened to a sweeping search light. The characteristic features of the radiation depend on two key parameters: the angular frequency ω_0 of the orbiting electron and $\gamma = \frac{Ee}{mc^2}$. The instantaneous direction of the radiation cone is that of the instantaneous velocity of the electron, and the opening angle of the cone is $\frac{1}{\gamma} = \frac{mc^2}{Ee}$. This is typically around 10^{-4}, or 0.1 mrad. The emitted spectrum is very broad, ranging from the far infrared to the hard X-ray region. However, the spectrum falls off quickly for photon frequencies higher than $\gamma^3\omega_0$ (Figure II.7). The angular frequency of an electron in the storage ring ω_0 is

typically of order 10^6 cycles per second, so the hard X-ray frequency cut-off is around 10^{18} cycles per second. We shall now show how one can understand these basic features from simple physical arguments. We analyse the simpler case of an electron travelling on a path comprised of short straight segments, with abrupt bends at points A, B, C, etc., as shown in Figure II.4. Subsequently the limit will be taken where the straight sections become infinitesimally small and the path becomes a circular arc. [2] In linear, uniform motion the electron does not radiate. At each bend it changes its velocity (but not its speed), and therefore it has a short period of acceleration during which it radiates. The observer is along the direction BC, and the time the electron spends in getting from one bend to the next is denoted $\Delta t'$. Consider in the top part of Figure II.4 the propagation of a wavefront emitted by the electron when passing the bend at B. During the time the electron spends in getting from B to C the wavefront has moved the distance $c\Delta t'$ towards the observer, at which point a new wavefront is emitted from C, which is $v\Delta t'$ closer to the observer than B. These two wavefronts will thus be $(c-v)\Delta t'$ apart, and the observer experiences that they arrive within a time interval

$$\Delta \mathrm{t} \ = \frac{(c \ - \ v)\Delta \mathrm{t}'}{c} = (1 \ - \ \beta_e)\Delta t' \tag{II.6}$$

where β_e is the ratio between the electron velocity and the speed of light. The same kind of arguments can be made for the pair of wavefronts emitted when the electron was at A and B; the only difference is that the distance travelled by the electron towards the observer is $v\Delta t' \cos\alpha$, α being the angle between the velocity and the direction to the observer. The wavefront from A is therefore not $(c-v)\Delta t'$ ahead of the wavefront emitted from B, but a distance $(c - v\ cos\alpha)\Delta t'$. In other words, the time compression of wavefronts – the Doppler effect – appears less pronounced to the observer. The time interval, Δt, between

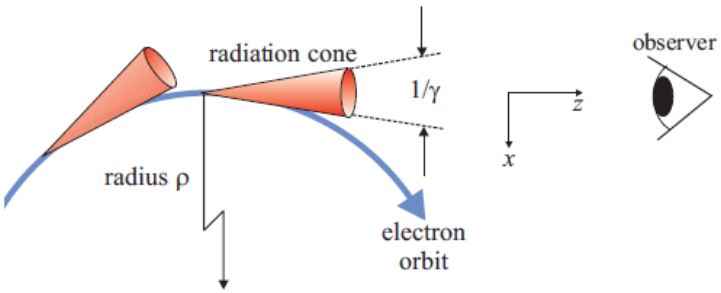

Figure II.3: Trajectory of an electron in a constant magnetic field. The radiation cone is the spatial limit of the emission of the bending magnets radiation for a relativistic electron. [2]

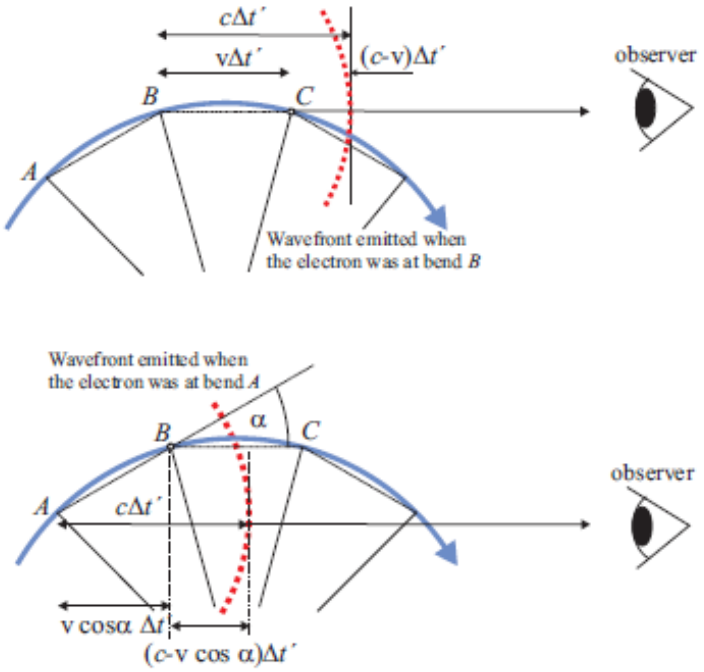

Figure II.4: Scheme of the trajectory of the electron. [2]

wavefronts measured by the observer is related to the time interval $\Delta t'$ by:

$$\Delta t \;=\; (1 \;-\; \beta_e \; cos \; \alpha)\Delta t' \tag{II.7}$$

Since β_e and $cos\,\alpha$ are both very close to unity they can be expanded

$$\Delta t \;\approx\; \left[1 - \left(1 \;- \frac{1}{2\gamma^2}\right)\left(1 - \frac{\alpha^2}{2}\right)\right]\Delta t' \tag{II.8}$$

which simplifies to read:

$$\Delta t \;\approx\; \left[\frac{1 + (\alpha\gamma)^2}{2\gamma^2}\;\right]\Delta t' \tag{II.9}$$

With $\alpha \;\approx\; 0$ and $\gamma \;\approx\; 10^4$ the time compression of the wavefronts experienced by the observer is enormous. The Doppler effect is in fact maximal when $\alpha = 0$, and has decreased by a factor of two when $\alpha \;=\; 1/\gamma$. This then explains why the natural opening angle of synchrotron radiation is of order γ^{-1}. Note that this is the opening angle in all directions. In the vertical plane the angular divergence is γ^{-1}, whereas in the horizontal plane the angular divergence of the fan of radiation depends on how long a segment of the circular arc is viewed by the observer. Taking the limit $\Delta t' \rightarrow \; 0$, the general relation between the observer time t and the retarded (or emitter) time t' is therefore given by the differential equation

$$\frac{dt}{dt'} = \; (1 \;-\; \beta_e \; cos \; \alpha) \tag{II.10}$$

where β_e is the electron velocity in units of c, and α is the angle between the instantaneous velocity and the direction to the observer.

To estimate the energy, $\mathcal{E}_{rad}$, radiated by the electron as it transits from A to C it is necessary to consider the power density of the radiated field. This is given by the magnitude of the Poynting vector $|\vec{S}| = B_{rad}E_{rad} = c\epsilon_0 {E_{rad}}^2$ rad with units of Wm^{-2}. $\mathcal{E}_{rad}$ can then be calculated by multiplying S by product the of the area of the radiated field at the observer, equal to $R^2\Delta\Omega$ with the solid angle $\Delta\Omega \sim \gamma^{-2}$, and the time interval Δt. Thus, the expression of the energy radiated is given by:

$$\mathcal{E}_{rad} = \frac{1}{4\pi}\frac{e^2}{4\pi\epsilon_0}\frac{\gamma}{\rho} \tag{II.11}$$

The number of photons emitted from the passage of a single electron, N_{rad}, is of order $E_{rad}/\hbar\omega_0$, and since the characteristic energy $\hbar\omega_0 \sim \hbar(\gamma^3 c/\rho)$, one obtains from Equation (II.11) that

$$N_{rad} \sim \frac{1}{4\pi}\frac{e^2}{4\pi\epsilon_0\hbar c} = \frac{1}{4\pi}\alpha \tag{II.12}$$

where $\alpha = \frac{e^2}{4\pi\epsilon_0\hbar c}$ is the fine structure constant. We can also use Equation (II.11) to obtain an expression for the power radiated by a current of electrons as it traverses a bending magnet. Equation (II.11) refers to the energy emitted from an electron path length of ρ/γ, so per unit length the energy is $\sim \gamma^4/\rho^2$. From Equation (II.5) we have $\rho \propto \mathcal{E}_e/B$, and as $\gamma \propto \mathcal{E}_e$, we obtain a dependence of ${\mathcal{E}_e}^2 B^2$. This result is in agreement with a full analysis which provides an expression for the total radiated power in practical units of

$$P[kW] = 1.266{\mathcal{E}_e}^2[GeV]\, B^2[T]\, L[m]\, I[A] \tag{II.13}$$

where L is the length of the electron trajectory through the bending magnet. The radiated power can be substantial, of order 1 MW for a third generation synchrotron, and has to be supplied to the electrons to keep them orbiting with the same energy.

3 Undulator Radiation

There is a much more efficient way to produce X-ray beams from a synchrotron than by having the electrons orbiting in a purely circular arc. In a typical storage ring there are straight sections followed by circular arc segments. In any one of these straight sections a device can be inserted that forces electrons to execute oscillations in the horizontal plane as it traverses through the section. This is achieved by an array of magnets which produces a field that alternates from up to down along the path. It is possible to construct an insertion device such that the radiation emitted by a given electron at one oscillation is in

phase with the radiation from the following oscillations. This implies that the amplitudes of the radiated waves are first added, and then the sum is squared to obtain the resulting intensity. An insertion device designed to operate in this way is known as an undulator. A necessary condition for the coherent addition of amplitudes is that electrons moving in an undulator execute small angular oscillations on a scale set by γ^{-1}. The coherent addition of amplitudes of different electrons implies a monochromatic spectrum (with harmonics), but one that is only quasi-monochromatic due to the finite number of periods in an undulator.

Although an undulator at a synchrotron has many desirable properties as a source of radiation it could nonetheless be improved upon considerably. The reason is that although the radiation from a single electron is coherent, in the sense that the radiation from one oscillation is in phase with that from the subsequent ones, the radiation from different electrons is incoherent. This results from the fact that the electrons traverse the undulator in a bunch without any positional order, in other words as an electron gas. If somehow the electrons in the bunch (or macro-bunch) could be ordered spatially into smaller micro-bunches (containing an average of N_q electrons $N_q > 1$), with a separation equal to the X-ray wavelength, then the radiation from one micro-bunch would be in phase with that from all of the following micro-bunches. It follows that the charge, eN_q, in a single micro-bunch would be much larger than e, and, since the micro-bunch is confined spatially within a distance shorter than the emitted wavelength, this charge can be considered as point like. In this case the brilliance would be enhanced by a factor of ${N_q}^2$ relative to a conventional undulator. [2] This is precisely what happens in a FEL. As shown in the Figure II.5, by changing the relative position between different arrays of magnets, the trajectory of the electrons may be tuned. The possible configurations are horizontal, vertical and helical. In the following the analytic description of the radiation emitted by a planar (horizontal or vertical) undulator will be presented briefly. A complete description can be found in [3][4][5].

The field of a planar undulator similar to the one reported in Figure II.6 in the plane $y = 0$, is:

$$\vec{B} = -B_0 sin(k_u z)\hat{e_y} \tag{II.14}$$

where B_0 is the maximum value of the magnetic induction field k_u is the undulator wave number expressed as in Equation (II.1), and $\hat{e_y}$ is the y-axis unit vector. The relativistic equation of motion of an electron of mass m_e and charge e moving in a magnetic field is:

$$\gamma m_e \dot{\vec{v}} = -e\vec{v}\times\vec{B} \tag{II.15}$$

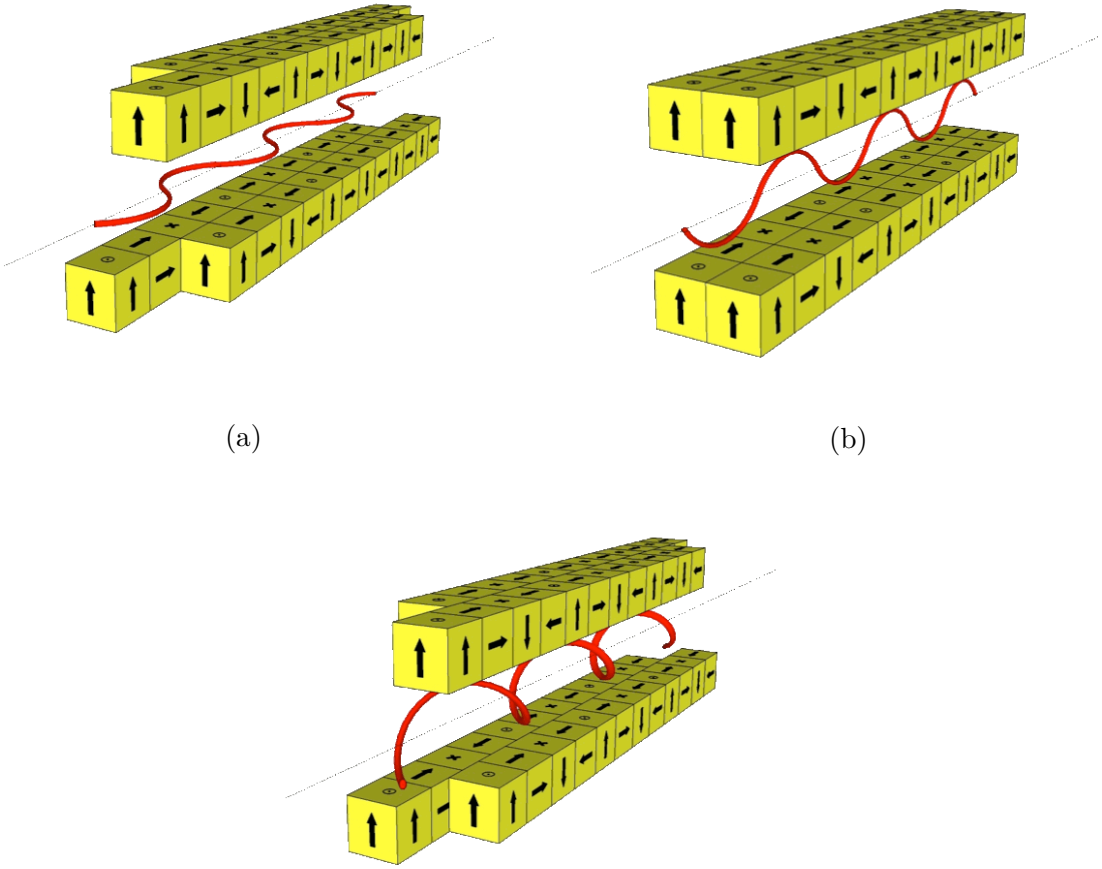

(a) (b)

(c)

Figure II.5: Illustration of the possible configurations of undulators: (a) horizontal, (b) vertical and (c) helical. The red line is the trajectory of the electrons. [6]

giving rise to the coupled equations:

$$\begin{cases} \ddot{x} = \frac{e}{\gamma m_e} B_y \dot{z} \\ \ddot{z} = -\frac{e}{\gamma m_e} B_y \dot{x} \end{cases} \tag{II.16}$$

The first order solution of the equations can be obtained considering $v_z \approx v = \beta c$, $x(0) = 0$ and $\dot{x}(0) = \frac{eB_0}{\gamma m_e k_u}$. In the reference frame of the undulator, this approximation leads to a sinusoidal trajectory:

$$x(z) = \frac{K}{\beta\gamma k_u} \sin(k_u z) \tag{II.17}$$

where K is the undulator parameter defined as:

$$K = \frac{eB_0}{m_e c k_u} \tag{II.18}$$

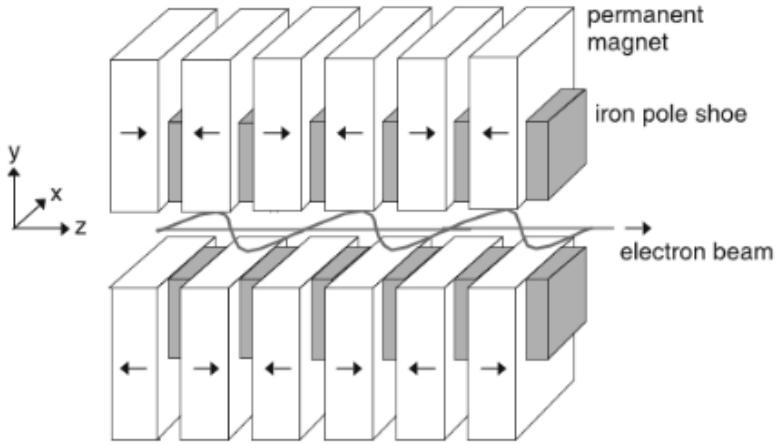

Figure II.6: Scheme of a planar undulator. [5]

As discussed in Section 2, the radiation emitted by a relativistic electron is mostly concentrated in a narrow cone with an opening angle $\frac{1}{\gamma}$, centred around the instantaneous tangent to the particle trajectory. According to the trajectory Equation (II.17), the tangent direction in a planar undulator varies sinusoidally with the angle respect to the x-axis, so:

$$\theta = -\frac{K}{\beta_e \gamma} \cos(k_u x) \tag{II.19}$$

The maximum value of the angle is:

$$\theta_{max} \approx \left.\frac{dx}{dz}\right|_{max} = \frac{K}{\beta\gamma} \tag{II.20}$$

If $K \leq 1$, the angular oscillations are smaller than $\frac{1}{\gamma}$ and different field contribution from different portion of the trajectory overlaps and interfere giving rise to a narrow spectral line and its harmonics (undulator condition). If $K > 1$, the angular oscillations are greater than the aperture of the emission cone, so that the emission of the same electron in two different points of the trajectories are incoherent. Using the relation between the angle θ and x, allow us to obtain the sinusoidal motion as a function of x.

$$z(x) = -\frac{K}{\gamma k_u} \sin(k_u x) \tag{II.21}$$

In order to calculate the wavelengths allowed in the undulator case ($K \leq 1$), it is mandatory to describe the length of the electron trajectory inside the array of magnets. The formula above can be written as:

$$z(x) = A \sin(kx) \tag{II.22}$$

where A is the amplitude of the oscillation and k the wave number. In the undulator case, we consider the condition $Ak << 1$. To calculate the trajectory we have to integrate:

$$S = \int ds = \int \sqrt{dx^2 + dz^2} = \int_0^{\frac{2\pi}{k}} dx \sqrt{1 + \left(\frac{dz}{dx}\right)^2} \tag{II.23}$$

Solving the integral, one obtains

$$S \cong \frac{2\pi}{k} + \frac{A^2 k\pi}{2} = \lambda \left(1 + \frac{\pi^2 A^2}{\lambda^2}\right) \tag{II.24}$$

In the undulator case, we know that $A = -\frac{K}{\gamma k_u}$ and $S = \lambda_u(1 + \frac{K^2}{4\gamma^2})$. In order to have constructive interference between two radiation emitted in different point of the trajectory, one has to consider two subsequent crests of the electron trajectory. Mathematically, it is obtained with the conditions $cT - \lambda_u cos\theta = \lambda_1$ and $T = S/v$. θ is the emission cone angle. The wavelength of the light emitted in the laboratory reference frame is:

$$\lambda_1 = \frac{\lambda_u}{2\gamma^2}\left(1 + \frac{K^2}{2} + \gamma^2\theta^2\right) \tag{II.25}$$

This is the equation of the fundamental harmonics of the undulator. It depends on K, which means that it is possible to tune the wavelength by varying B_0, i.e. acting on the distance between the magnets. The undulator radiation presents also higher harmonic contribution with an angular distribution: on-axis emission ($\theta = 0$) presents only odd harmonics while off-axis emission ($\theta \neq 0$) has also even harmonics, which are less intense. The emission wavelength at higher harmonics can be estimated as

$$\lambda_n = \frac{\lambda_1}{n} \quad \text{n} = 1, 2, 3 \ldots \tag{II.26}$$

where n is the harmonic we want to consider. In Figure II.7, the emitted intensity of different insertion device is shown.

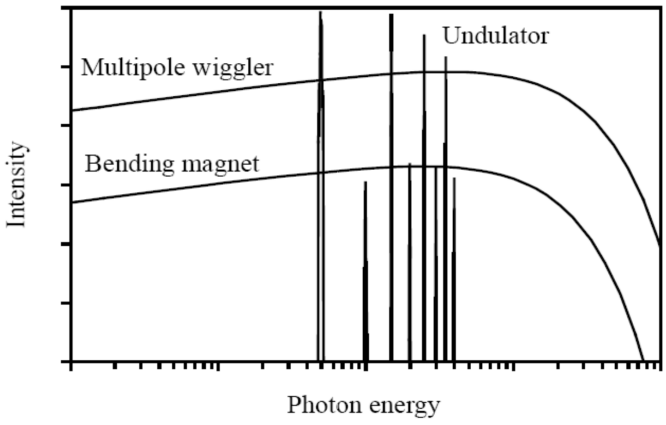

Figure II.7: Schematic illustration of the different wavelength emitted by bending magnets, wigglers and undulators.

4 High Gain Free Electron Lasers

The FEL radiation process starts with an electron bunch being injected into an undulator, with a velocity close to the speed of light and a uniform density distribution within the bunch. In the undulator the electrons are wiggled and emit light characteristic of the undulator strength but within a certain energy bandwidth. In a high gain FEL the emitted intensity grows because a large number of particles radiate coherently. The intensity of the emitted electromagnetic radiation grows quadratically with the number of coherently radiating particles i.e. $I_N = N^2 I_1$. The ideal case is represented by N particles concentrated in a region smaller than the radiation wavelength. This would behave like a macro particle of charge $Q = -Ne$. Electrons losing energy to the electron magnetic wave travel on larger sinusoidal trajectory, while the opposite is true for electron gaining energy from the electromagnetic wave. This result in a modulation in the longitudinal velocity, which ultimately bring to spatial modulation and concentration of the charge in the bunch. This process is called microbunching, shown in Figure II.8. The structured electron beam amplifies only certain photon energies (Equation (II.25)) at the cost of kinetic energy until the system goes into saturation. The micro-bunch structuring reduces the phase space available to the photons, thus they are also more likely to have a similar phase and the emitted beam is coherent. Since X-rays are electromagnetic waves, one should expect some kind of refraction phenomena at interfaces between different media as lower energy radiation does (e.g. Infrared (IR)). To describe such refractive phenomena, the media of interest are taken to be homogeneous with sharp boundaries between them, each having its own refractive index n. By definition the refractive index of vacuum is one. It is well known that for visible light in glass n is large and can vary considerably, ranging from 1.5 to 1.8 depending on the type of glass. This of course enables lenses to be designed for focusing light and thereby obtaining magnified images. For X-rays the difference from unity of n is very small, of order 10^{-5}. For X-rays, the refractive index can be expressed as

$$n \;=\; 1 \;-\; \delta \;+\; i\beta \tag{II.27}$$

where δ is of order 10^{-5} in solids and only around 10^{-8} in air. The imaginary part β is usually much smaller than δ. The refractive index is almost equal one. This means that the reflection angle is close to 90°. In other words, the variation in direction between the impinging X-ray and the reflected one is small. It is very difficult to change the direction of an X-ray. In practice, this forced to use a different geometry with respect to the circular one, typical of the synchrotron radiation. [2] The lack of proper optics prevents the development of an optical cavity for the EUV/soft x-ray spectral region. Thus, the production of the FEL radiation has to happen in a single pass through a long undulator.

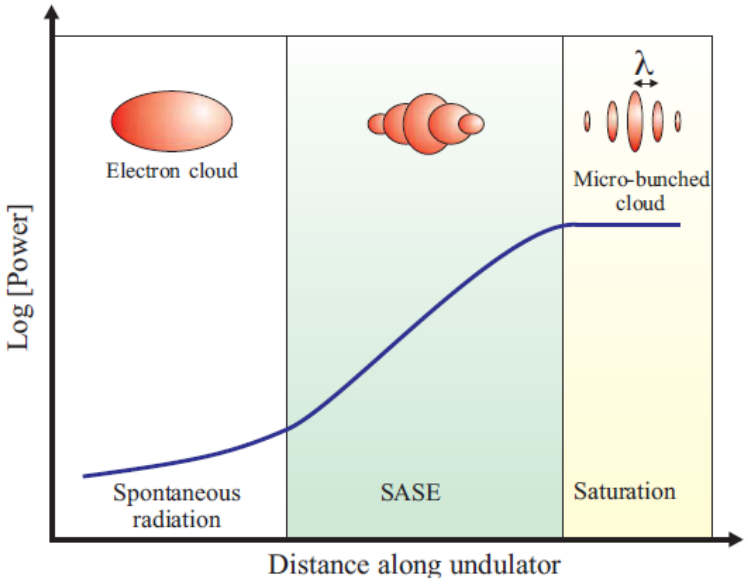

(a)

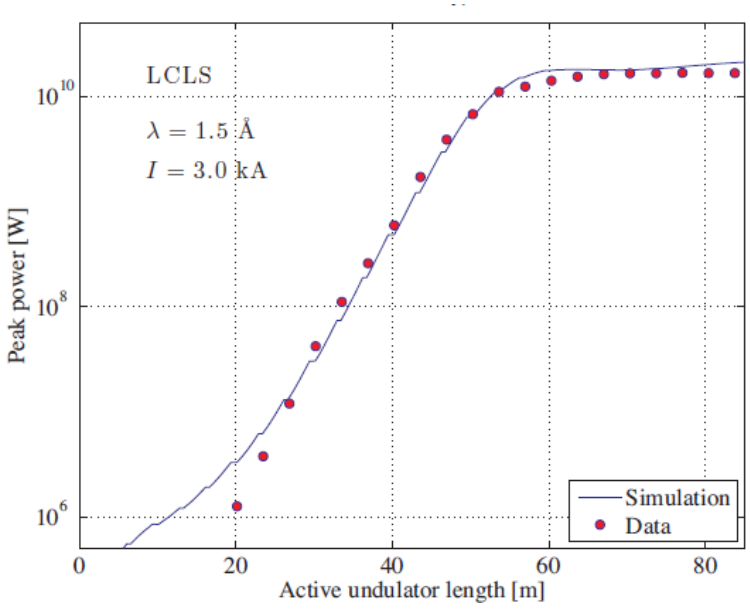

(b)

Figure II.8: (a) schematic of the power radiated by an electron cloud as it traverses through a long undulator. For short distances along the undulator there is no correlation between the radiation emitted by the different electrons in the cloud. Each electron emits as a coherent source, and the power of the 'spontaneous radiation' is proportional to the number of electrons in the cloud. Further downstream the electrons start to form micro-bunches and the SASE effect switches on, leading to an exponential growth in power. Eventually a train of micro-bunches forms with a spacing equal to the X-ray wavelength, and once this train is fully formed the intensity saturates; (b) red points, the measured power emitted from the LCLS as a function of undulator length; blue line, the results of a simulation of the power expected from the known parameters of the electron beam. [2]

A key concept validated also by experimental data [7], is that at saturation the microbunching structure is fully developed (Figure II.8b). This concept is a pillar of the working scheme of the FERMI FEL. In this case, saturation means that no more power can be extracted by the electron bunch and the energy starts to oscillate back and forth to the electron bunch. The analytical description of the charge modulation and the microbunching go beyond the scope of the present work. A complete description may be found in [5].

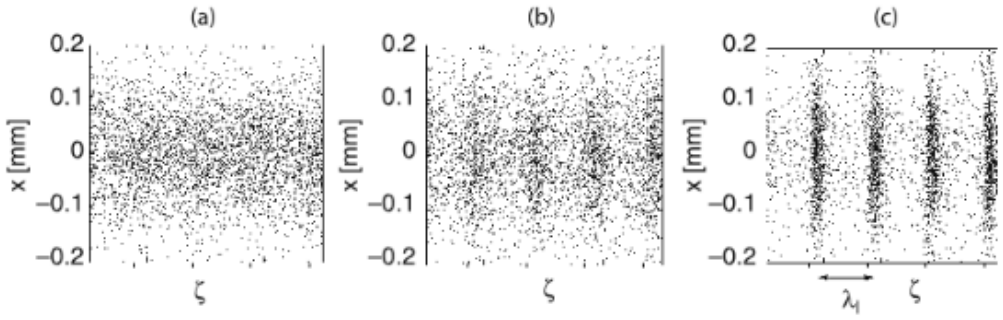

Figure II.9: Simulation of the microbunching process. x is the displacement from the undulator axis and ς is the internal coordinate, defined as $\varsigma = \frac{\psi + \frac{\pi}{2}}{2\pi} \lambda_l$. [5]

5 FERMI

FERMI is a seeded Free Electron Laser (FEL) facility located at the Electra laboratory in Trieste, Italy (Figure II.10). It is based on the principle of high gain, harmonic generation FEL amplifier employing multiple undulators, up-shifting and initial seed signal in a single-pass. FERMI is designed to operate in the EUV/ soft X-rays range (4-100 nm wavelength). This range is divided in two subgroups: FEL-1, which operates between 20 and 100 nm delivering sub 100 fs pulses with 10^{13} photons per pulse; FEL-2, which cover the lower wavelength range (4-20 nm). In FEL-2 the pulse generated by FEL-1 is used to seed a new electron bunch, thus pushing toward higher energy the laser emission. [8] In Table II.1 the main parameters of FEL-1 and FEL-2 are reported. In this section the structure of the machine is briefly described. A complete description of FERMI can be found in [8][9].

Parameters	Value @ 40nm	Value @ 10nm (fresh bunch)	Units
Electron beam energy	1.2	1.2	GeV
Peak current	800	500	A
Emittance (slice)	1.5	1.5	μm, rms
Energy sprea (slice)	150	150	keV
Bunch duration	700	1400	fs, FWHM
Repetition rate (so far)	10	10	Hz
FEL peak power	1-5	0.5-1	GW
FEL pulse duration	50-100	100-200	fs
Photon/pulse	10^{14}	10^{12}	GeV
Bandwidth	20	5	meV

Table II.1: Main parameters for FEL-1 and FEL-2, respectively.

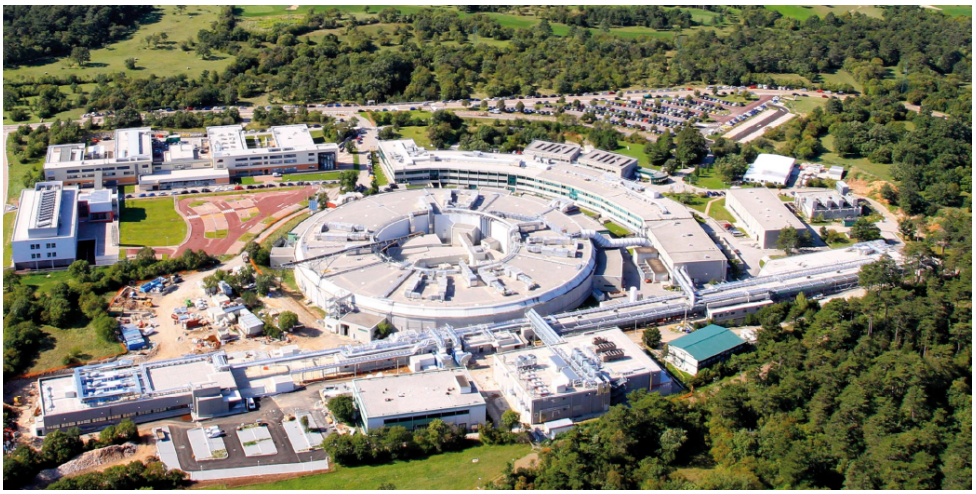

Figure II.10: Elettra-Sincrotrone Trieste facility.

5.1 Photoinjector and LINAC

Before the FEL emission takes place, it is mandatory to generate an electron bunch and accelerate it to reach the resonant energy. At FERMI, the generation of the electron bunch is obtained with a UV laser which impinges on a copper photocathode. At first, the bunch is accelerated with a photoinjector. At the end of the photoinjector, the bunch has an energy around 100 MeV. Then the acceleration takes place in the Linear Accelerator (LINAC). The LINAC is divided into four stages of conductive travelling acceleration sections (S-band) operating at 3GHz. In the middle of the first stage, there is an Radio

Frequency (RF) structure, which allows the temporal decrease from 10 ps to 700 fs, in combination with the first beam compression section. Each stage accelerates the electron bunch, which is compressed a second time before the last stage. At the end of the LINAC, the energy of the electrons is 1.2 GeV (FEL-1) and 1.5 GeV (FEL-2). [10] [11] Figure II.11 shows a scheme of the main linear accelerator of FERMI.

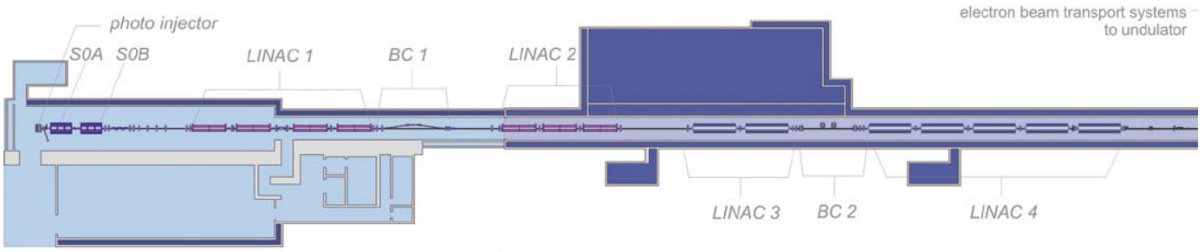

Figure II.11: Scheme of the main LINAC of FERMI. [8]

5.2 Undulators and Photon Transport

At the end of the LINAC, the electron beam is transported with bending magnets. In this part of the machine, the beam is sent to the desired undulator section (FEL-1 or FEL-2). The two undulator lines are parallel. The energy modulation induced by the interaction of the seed laser with the electron beam in the first undulator (the "modulator") is converted to spatial modulation by passing the beam through the magnetic field of a dispersive section. The bunching further increases the initial bunch modulation at harmonics of the seed wavelength. Thus, re-bunched, the electrons emit coherent radiation in a second undulator (the "radiator") tuned at a higher harmonic corresponding to the desired FEL output. This scheme broadly describes the FEL-1 layout, down to 20 nm. To reach the shortest design wavelength of 4 nm, a second stage (modulator + dispersive section + radiator) is added to produce the FEL-2 configuration. The modulators for both FEL-1 and FEL-2 have fixed, linear polarization. They must be tunable in the 240-360 nm range, a requirement that can be satisfied by a wide range of period lengths among which the shortest acceptable, 10 cm, is favoured for FERMI. The first stage radiator and the second stage modulator for FEL-2 are also designed for fixed linear polarization. All the other undulators are of the variable polarization type, based on the widely used APPLE-II (Advanced Planar Polarized Light Emitter) configuration, the most efficient one for this application (Figure II.12). All polarizations are tunable over the full design tuning ranges of 100 to 20 nm and 20 to 4 nm of FEL-1 and FEL-2 respectively. Dedicated correction coils at both ends of each individual undulator magnet compensate the residual random magnetic field errors as well as the misalignment effects. [8] At the exit of the last undulator the electrons are deviated to a beam dump (used for the end station TeraFERMI). The

photons instead are transported to the end stations through the Photon Analysis Delivery and Reduction System (PADReS). A full description of the photon transport can be found in [12]. Before exiting the safety hutch, there is a physical shutter that blocks mechanically the beam.

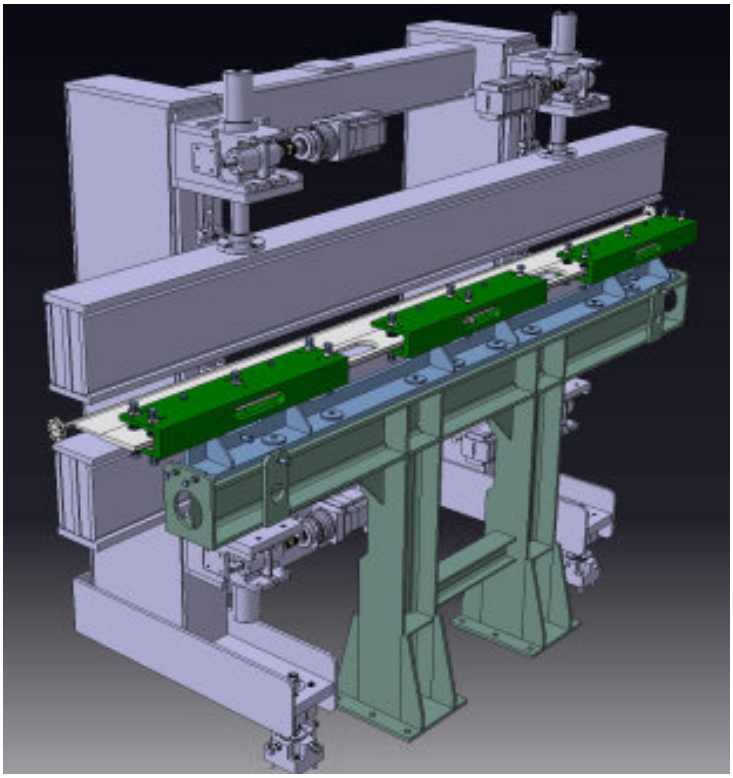

Figure II.12: One Apple II undulator in the vacuum chamber. [8]

5.3 Beamlines

The choice of harmonic generation by an external seed laser is dictated by the scientific applications and the flexibility that such choice entails. As the seed laser determines the duration, bandwidth, and wavelength of the output radiation, all are tunable and controllable, covering a wide spectral range. The choice of design parameters, in fact, allows FERMI to generate FEL radiation with a wide range of characteristics tailored to match a diversity of experimental requirements, ranging from single shot, short ($\sim 100 fs$), high brilliance, time-resolved experiments to ultra-fast pump-probe experiments, to high resolution (1 – 5 meV) experiments with close to transform-limited radiation on the ps time scale. The seed laser furthermore provides a reference signal throughout the FERMI facility (including the experimental beamlines) to facilitate the femtosecond level precision timing and synchronization of all systems. [6] At the present state there are six beamlines at FERMI.

1. EIS-TIMEX generates and probes high energy density thermodynamic regimes. To achieve these metastable conditions, it reaches high fluxes and sub-ps time resolution. To do so, the high peak power of the FERMI FEL source is used to induce an ultrafast and almost isochoric heating. The energy deposited in the sample forced the material under nonequilibrium condition characterized by hot electrons and cold lattice.

2. EIS-TIMER is devoted to exploit the transient grating approach. It is a FEL- based four-wave-mixing instrument, which allow also the study of the machine properties.

3. DiProI is dedicated to Resonant Coherent Diffraction Imaging.

4. MagneDyn is devoted to study ultrafast time resolved and pump-probe magneto-optic spectroscopies. It is designed for experiments on transient magnetic states of matter.

5. LDM is dedicated to the investigation of Low-Density Matter, such as atoms, molecules, clusters, and gases.

6. TeraFERMI is the only beamline that operates continuously because it exploits the broadband radiation emitted from the electron bunch in the beam dump after the undulator chain.

The experiment described in this work was fully developed and carried out in the EIS – TIMEX end station.

Chapter III

Interaction of Sub-ps Laser Pulses and Electron Bunches with Condensed Matter

In this Chapter, the interaction of EUV sub-ps photon pulses and compressed electron bunches with condensed matter is discussed. The successful implementation of lasing at such short wavelengths has led to several advantages over conventional visible lasers. In fact, visible tabletop lasers have frequencies under the resonant frequency of plasmas ω_p. As shown in Section 1, the energy deposition inside the material requires a laser with frequency above ω_p. The radiation is reflected otherwise.

Pulsed Laser Ablation

Lasers incident on solid targets cause melting and expansion leading to the removal of material, referred to as ablation. Laser systems with pulse durations variable from about 100 fs to several nanoseconds have become available. These lasers allow one to perform a detailed analysis of the laser-matter interaction at different laser pulse durations, leaving the other laser parameters almost unchanged. Since at very short time scales thermal conduction into the target can be neglected (to a first approximation). Thus, laser ablation with femtosecond and picosecond laser pulses can be considered as a direct solid-vapour transition. In contrast, in nanosecond laser heating of metals the absorbed laser energy first heats the target to the melting point and then to the vaporization temperature [13].

In the analysis of the laser-ablation process with very intense picoseconds laser pulses or shorter, it is useful to consider the adiabatic approximation. In this case, the laser absorption and the induced phenomena of target heating, vaporization, and plasma

formation take place much faster than the expansion of the ablated material. Thus, the laser-ablation process can be divided into two stages: (a) evaporation of the solid target and plasma formation; (b) expansion of the ablated plume in vacuum or into the surrounding medium. The adiabatic approximation is equivalent to the following simplified image of the ablation process: first, the laser energy is converted into internal energy of the target and plasma plume; second, the absorbed laser energy is partially transformed into kinetic energy of the ablation plume. By using the adiabatic approximation, relatively simple analytical and numerical models can be used for describing the plasma formation and expansion.
The raw data of our experiment (Figure V.9) were single-shot diffraction images, obtained with 100 keV electron bunches (Chapter IV, Section 3). Therefore, the last section describes briefly the electron diffraction.

1 Fundamentals of Plasma Physics

Laser radiation has an inherently large energy density when focused, which typically leads to a fast rise in temperature of any matter upon which it is incident. Matter rapidly undergoes a phase transition to a plasma when subjected to intense laser light, regardless of its starting phase. [14] A plasma is a fluid state of matter which exists at high temperatures or densities. The characteristic difference between a plasma and a condensed fluid, such as a liquid or gas, is that matter no longer occupies the lowest possible energy states. In conventional plasmas, energetically favourable molecular bonds break, electrons in atoms become excited to high energy levels or become ionized completely. Therefore, a plasma inevitably contains many types of charged particles, free to move independently. This fact allows the description of the charged system as a gas. Moreover, a metal can be considered a cold plasma, where the free charges are the electrons in the conduction band. Before the description of plasma frequency, we have to introduce the dielectric function.

1.1 Dielectric Function

The dielectric constant ϵ of electrostatic is defined in terms of the electric field $\vec{E}$ and the polarization $\vec{P}$, which is the dipole moment density:

$$\vec{D} = \epsilon_0 \vec{E} + \vec{P} = \epsilon \epsilon_0 \vec{E} \tag{III.1}$$

Thus defined, ϵ is also known as the relative permittivity. [15] The introduction of the displacement $\vec{D}$ is motivated by the usefulness of this vector related to the externally applied charge density ρ_{ext} in the same way as $\vec{E}$ is related to the total charge density

$\rho = \rho_{ext} + \rho_{ind}$, where ρ_{ind} is the charge density induced in the system by ρ_{ext}. Thus, the divergence relation of the electric field is:

$$\nabla \cdot \vec{D} = \nabla \cdot \epsilon\epsilon_0 \vec{E} = \rho_{ext} \tag{III.2}$$

$$\nabla \cdot \vec{E} = \frac{\rho}{\epsilon_0} = \frac{(\rho_{ext} + \rho_{ind})}{\epsilon_0} \tag{III.3}$$

In the case of an electron gas, the dielectric function is strongly dependent on the frequency and the wavevector of the electrons, so $\epsilon = \epsilon(\omega, \vec{K})$. In the following, it is necessary to consider the relations between the Fourier components of $\vec{D}$, $\vec{E}$, and ρ. For brevity, consider only the dependence concerning to the wavevector. Define $\epsilon(\vec{K})$ such that:

$$\vec{D}\left(\vec{K}\right) = \epsilon\left(\vec{K}\right)\vec{E}(\vec{K}) \tag{III.4}$$

then, the divergence relations become:

$$\nabla \cdot \vec{D} = \nabla \cdot \sum \epsilon\left(\vec{K}\right)\vec{E}(\vec{K})e^{i\vec{K}\cdot\vec{r}} = \sum \frac{\rho_{ext}(\vec{K})}{\epsilon_0} e^{i\vec{K}\cdot\vec{r}} \tag{III.5}$$

$$\nabla \cdot \vec{E} = \nabla \cdot \sum \vec{E}(\vec{K})e^{i\vec{K}\cdot\vec{r}} = \sum \frac{\rho(\vec{K})}{\epsilon_0} e^{i\vec{K}\cdot\vec{r}\rightarrow} \tag{III.6}$$

Each of the equations must be satisfied term by term; we divide one by the other to obtain

$$\epsilon\left(\vec{K}\right) = \frac{\rho_{ext}(\vec{K})}{\rho(\vec{K})} = 1 - \frac{\rho_{ind}(\vec{K})}{\rho(\vec{K})} \tag{III.7}$$

1.2 Plasma Optics

Having conduction electrons free to move, metals can be described as a cold plasma, where the plasma is a free electron gas and the ion, moving 10^3 times slower can be considered as they stay still. This approximation is called Born Oppenheimer approximation. According to this, the electronic system can be considered independent of the ion system. The long-wavelength dielectric response $\epsilon(\omega, 0)$ of an electron gas is obtained from the equation of motion of a free electron in an electric field:

$$m\frac{d^2\vec{x}}{dt^2} = -e\vec{E} \tag{III.8}$$

If x and $\vec{E}$ have the time dependence $e^{-i\omega t}$, then:

$$-\omega^2 m\vec{x} = -e\vec{E}\ ; \vec{x} = e\vec{E}/m\omega^2 \tag{III.9}$$

The dipole moment of one electron is $-e\vec{x} = e^2\vec{E}/m\omega^2$, and the polarization, defined as the dipole moment per unit volume, is

$$\vec{P} = -nex = -\frac{ne^2}{m\omega^2}\ \vec{E} \tag{III.10}$$

where n is the electron concentration. The dielectric function at frequency ω is

$$\epsilon(\omega) = \frac{D(\omega)}{\epsilon_0 E(\omega)} = 1 + \frac{P(\omega)}{\epsilon_0 E(\omega)} \tag{III.11}$$

Using the Equation (III.10) of the polarization of the free electron gas, the dielectric function becomes

$$\epsilon(\omega) = 1 - \frac{ne^2}{\epsilon_0\, m\omega^2} \tag{III.12}$$

The plasma frequency ω_p is defined by the relation $\omega_p = \frac{ne^2}{\epsilon_0\ m}$. A plasma is a medium with an equal concentration of positive and negative charges, of which at least one charge type is mobile. In a solid, the negative charges of conduction electrons are balanced by an equal concentration of positive charge of the ion cores [16]. We write the dielectric function as

$$\epsilon(\omega) = 1 - \frac{\omega_p^2}{\omega^2} \tag{III.13}$$

If the positive ion core background has a dielectric constant labelled $\epsilon(\infty)$ essentially constant up to frequencies well above ω_p, then the equation becomes

$$\epsilon(\omega) = \epsilon(\infty) - \frac{ne^2}{\epsilon_0\, m\omega^2} = \epsilon(\infty)\left(1 - \frac{\overline{\omega}_p^2}{\omega^2}\right) \tag{III.14}$$

where $\overline{\omega}_p$ is defined as $\overline{\omega}_p^2 = \frac{ne^2}{\epsilon_0\epsilon(\infty)\ m}$. Notice that $\epsilon = 0$ at $\overline{\omega}_p = \omega_p$.

1.3 Dispersion Relation

In a non-magnetic isotropic medium, the electromagnetic wave equation is

$$\mu_0 \frac{\partial^2 \vec{D}}{\partial t^2} = \nabla^2 \vec{E} \tag{III.15}$$

where μ_0 is the magnetic permittivity of vacuum. Considering that $\vec{E} \propto e^{i\vec{K}\cdot\vec{r} - i\omega t}$, the dispersion relation for electromagnetic waves is:

$$\epsilon\left(\omega, \vec{K}\right)\epsilon_0\mu_0\omega^2 = K^2 \tag{III.16}$$

This equation implies several physical consequences. If ϵ and ω are real and $\epsilon > 0$, then K is real and a transverse electromagnetic wave propagates with the phase velocity $c/\sqrt{\epsilon}$. If ϵ and ω are real but $\epsilon < 0$, then K is imaginary and the wave is damped with a characteristic length $1/|K|$. If ϵ is complex and ω is real, then K is complex, and the waves are damped in space (Figure III.1). I will describe only the transverse optical modes in a plasma because it is strictly related to the reason why it is important to use Extreme Ultraviolet (EUV) and soft X-rays to deposit energy in a sample. The other cases can be found in [16].

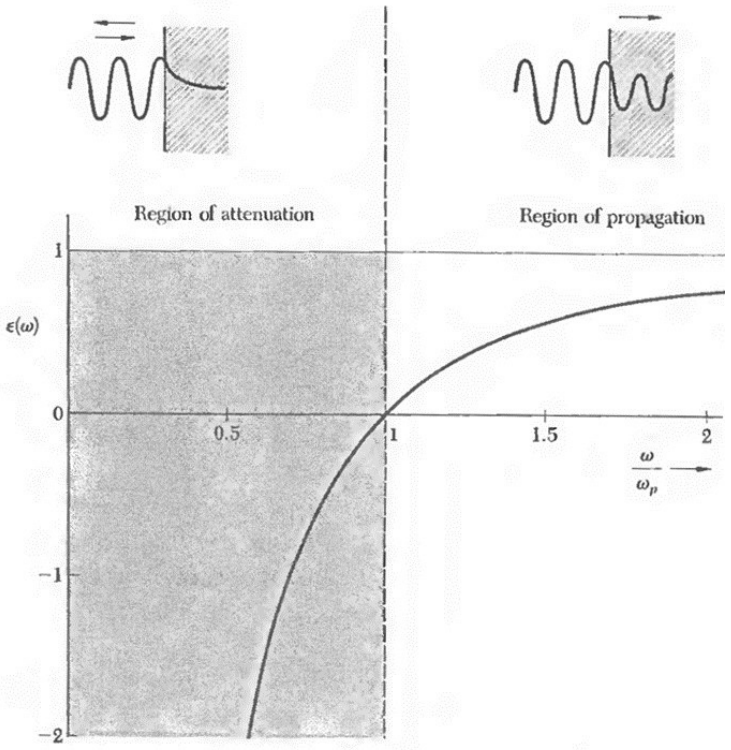

Figure III.1: Dielectric function $\vec{\epsilon}(\theta)$ of a free electron gas versus frequency in units of the plasma frequency. Electromagnetic waves propagate when ϵ is positive and real. They are reflected otherwise. [16]

1.4 Transverse Optical Modes in a Plasma

The dispersion relation in Equation (III.16) becomes, with Equation (III.14) for $\epsilon(\omega)$,

$$\epsilon(\omega)\,\omega^2 = \epsilon(\infty)\left(\omega^2 - \overline{\omega}_p^2\right) = K^2 \tag{III.17}$$

For $\omega < \overline{\omega}_p$ we have $K^2 < 0$, so that the wavevector is imaginary. The solutions of the wave equation are of the form $e^{-|K|x}$ in the frequency region $0 < \omega < \overline{\omega}_p$. Waves incident on the medium in this frequency region do not propagate but will be totally reflected. An electron gas is transparent when $\omega > \overline{\omega}_p$, from here the dielectric function is positive real. If the frequency is above the resonant frequency $\overline{\omega}_p$, the radiation can propagate in the medium (Figure III.1). This condition is necessary in order to deposit energy inside the sample. The dispersion relation in this region may be written as

$$\omega^2 = \overline{\omega}_p^2 + \frac{K^2}{\epsilon(\infty)} \tag{III.18}$$

this describes transverse electromagnetic waves in plasma. The dispersion relation (Equation (III.18)) implies that when an electromagnetic wave is incident on a plasma, it is reflected if its frequency is below the plasma frequency. Consequently, for a given frequency

of radiation, there is a critical electron density above which it cannot propagate. This critical density for a given photon energy ϵ_γ is given by

$$n_c[10^{23}cm^{-3}] = 7.252 \times 10^{-3} \left(\epsilon_\gamma[eV]\right)^2 \tag{III.19}$$

Visible light ($\epsilon_\gamma \sim 2eV$) is reflected at densities of around $10^{21}cm^{-3}$. Therefore, in most laser plasma experiments, light is reflected from an outwardly expanding low density plasma plume and heat is conducted to the main target by electrons. Plasmas at solid material densities ($n_e > 10^{23}cm^{-3}$) can only be created and heated directly by photons in the EUV range or above ($\epsilon_\gamma \gtrsim 12eV$).

1.5 FEL as Suitable Pump for Ultrafast Processes in Metals and Insulators

From the preceding discussion on the dielectric function, we conclude that to deposit energy inside a metal, we need a radiation in range on EUV and soft-x-rays. Being the radiation pulse of the order of 100 fs, EUV FEL pulses induce heating of the electron system well before excitation of the ion thermal motion. When EUV FEL pulses are absorbed by a sample material they can promote electrons from the valence band to the conduction bands or if the energy is sufficient they can ionize the atom. The time scale of this process is of the order of 10 fs. The excitation of the ion requires more time (ps). The hot electrons, once excited by the Free Electron Laser (FEL) pump, interacts with the lattice through electron-phonon interaction. This difference in time allows to consider two different systems: hot free electrons and cold lattice. According to this, it is possible to consider hot electrons and the cold lattice as two independent systems. Thermodynamically, it can be described with a Two Temperatures Model (TTM) [17] [18], in which two different temperatures are associated with the electronic system and ionic system, respectively. The extremely short duration of the FEL pulse triggers isochoric heating in the sample. While the electronic system absorbs the laser, the ion system is unchanged.

In this work, we carried Ultrafast Electron Diffraction (UED) with FEL pump on gold single crystal and polycrystalline samples and diamond single crystal. Being the diamond an electrical insulator, the theoretical description above cannot be applied. However, even in this case, EUV radiation is more suitable to efficiently deposit energy on the sample material. EUV and soft-x-ray radiation have energy comparable or greater than to the band gap between the valence band and the conduction band (e.g. $E_{gap\ diamond} = 5.47eV$

[19]). Therefore, pumps of this kind can promote electrons to the conduction band. In particular, the diamond is transparent to visible light, while it absorbs EUV radiation (Figure III.2). So that, a high energy density source such as FERMI FEL is needed in order to heat the samples through the absorption of the energy of the pump by the electronic system.

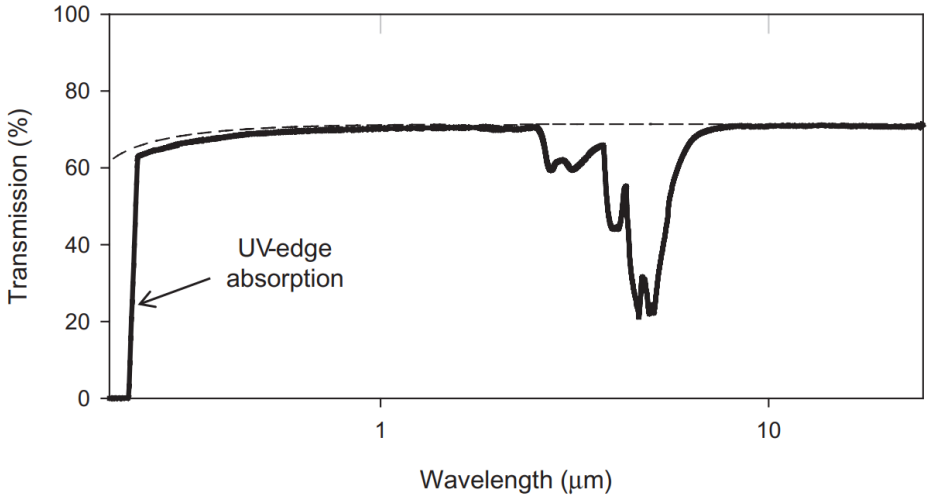

Figure III.2: Transmission of diamond as a function of the wavelength of the incident radiation. In the EUV region, an absorption edge is present. [20]

2 Electron Diffraction

One of the possible approaches to investigate the melting of a sample at the microscopic level is to detect the diffraction peaks in time [21]. In fact, during the melting phase transition, the long-range atomic order is lost. Therefore, the melting process is revealed as a lowering and widening of the diffraction peaks. In this section, the interaction between an electron and the lattice and the diffraction conditions are briefly described [22] [23].

2.1 Elastic Scattering

When an electron passes close to an atom it interacts with the atom's nucleus through the Coulomb force, leading to scattering of the electron. Generally, two types of scattering are discerned: elastic scattering, where the momentum of the electron is changed, while the energy change is insignificantly small; inelastic scattering, where both the electron's energy and momentum are changed. If an electron elastically scatters it radiates and loses some energy. However, this energy loss is very small and can be neglected in diffraction

theory: the velocity and the wavelength of the electron are assumed to be unaltered after the elastic scattering event.

2.1.1 Scattering on a Single Atom

We start by describing one electron as a wave that scatters on a single atom positioned at $\vec{r_0}$. The incoming wave is usually assumed to be a plane wave as it comes from a distant source. The outgoing wave is described as a spherical wave originating from the atom on which the electron scatters. The total wave is a linear combination of the scattered and unscattered wave.

$$\psi\left(\vec{r}\right) = \psi_0 \left[e^{i\vec{k_0} \cdot \vec{r}} + f\left(\Delta\vec{k}\right) \frac{e^{i\vec{k} \cdot (\vec{r} - \vec{r_0})}}{(\vec{r} - \vec{r_0})} \right] \tag{III.20}$$

where $f\left(\Delta\vec{k}\right)$ is the scattering amplitude, and $\Delta\vec{k} = \vec{k} - \vec{k}_0$, with $\vec{k}_0$ the wavevector of the incoming wave and $\vec{k}$ the wavevector of the outgoing wave. Note that for elastic scattering $\vec{k} = \vec{k}_0 = k$ and only the angle $\theta = 2\arcsin(\Delta\vec{k}/2\vec{k_0})$ between the incoming and outgoing wave is relevant. The time-dependency $e^{-i\omega t}$ is left out for convenience. To solve the Schrödinger equation for the total wave function, usually the (first) Born approximation is applied, which assumes that the total wave ψ does not differ too much from the incident wave ψ_0, and that the wave is scattered only once by the material [24] [25]. When also assuming that the scatterer is small compared to the distance to the detector, i.e. $|\vec{r} - \vec{r_0}| \approx |\vec{r}|$, the wave function is given by

$$\psi\left(\vec{r}\right) = \psi_0 \left[e^{i\vec{k_0} \cdot \vec{r}} + f\left(\theta\right) \frac{e^{i\vec{k} \cdot \vec{r}}}{|\vec{r}|} \right] \tag{III.21}$$

with the scattering amplitude

$$f\left(\theta\right) \approx -\frac{m}{2\pi\hbar^2} \int e^{i\Delta\vec{k} \cdot \vec{r}_0} V_{at}\left(\vec{r}_0\right) d^3\,\vec{r}_0 \tag{III.22}$$

where m is the electron mass, $\hbar$ is the reduced Planck constant, and $V_{at}\left(\vec{r}_0\right)$ is the scattering potential of the atom. Equation (III.22) shows that the scattered wave is proportional to the Fourier transform of the scattering potential. It is this principle that is used in diffraction experiments. In case of a periodic potential (i.e. periodically arranged atoms), constructive interference can occur. When scattering on N_{at} atoms at positions $\vec{R}_j$ the scattering potential has to be replaced by $V\left(\vec{r}\right) = \sum_{j=0}^{Nat} V_{at,\ \vec{R}_j}\left(\vec{r} - \vec{R}_j\right)$ where$V_{at,\ \vec{R}_j}$ is the scattering amplitude of the specific atom at position $\vec{R}_j$. The total scattering amplitude is then simply the sum of all atomic scattering amplitudes $f_{at,\ \vec{R}_j}$. The quantity measured is the probability for scattering over an angle θ, which is given by

$$P_{scatt}\left(\theta\right) = \psi^*\psi \propto \left| \sum_{j=1}^{N_{at}} f_{at,\ \vec{R}_j}\left(\theta\right) e^{-i\Delta\vec{k} \cdot \vec{R}_j} \right|^2 \tag{III.23}$$

2.1.2 Scattering on a Crystal

Because of the periodicity in a crystal, a unit cell can be defined that consists of a single atom, a single molecule, multiple atoms, or multiple molecules. The origins of the unit cells are given by $\vec{r}_g = m\vec{a}_1 + n\vec{a}_2 + p\vec{a}_3$, where $\{m, n, p\} \in \mathbb{Z}$, and $\vec{a}_1$, $\vec{a}_2$, and $\vec{a}_3$ are the primitive vectors that span the crystal. In a mono-atomic crystal the positions $\vec{R}_j$ of the atoms, as introduced in Section 2.1.1, are precisely $\{\vec{r_g}\}$. Combining this with Equation (III.23) it follows that the scattering intensity is maximum when

$$\Delta\vec{k} \cdot (m\vec{a}_1 + n\vec{a}_2 + p\vec{a}_3) = q2\pi \tag{III.24}$$

with $q \in \mathbb{Z}$. If the unit cell contains more than one atom the position of the k-th atom in the unit cell is given by $\vec{r}_k = u_k\vec{a}_1 + v_k\vec{a}_2 + w_k\vec{a}_3$, and the position of the atom in the lattice is given by $\vec{R}_j = \vec{r_g} + \vec{r_k}$. The scattered part of the wave function yields

$$\psi_{scatt}\left(\Delta\vec{k}\right) \propto \sum_{\vec{r_g}} \sum_{\vec{r_k}} f_{at}\left(\vec{r_g} + \vec{r_k}\right) e^{-i\Delta\vec{k} \cdot (\vec{r_g} + \vec{r_k})} \tag{III.25}$$

$$= \sum_{\vec{r_k}} f_{at}\left(\vec{r_k}\right) e^{-i\Delta\vec{k} \cdot \vec{r_k}} \sum_{\vec{r_g}} e^{-i\Delta\vec{k} \cdot \vec{r_g}} \tag{III.26}$$

$$= \mathcal{F}\left(\Delta\vec{k}\right) S\left(\Delta\vec{k}\right) \tag{III.27}$$

where in the second line the periodicity of the crystal is used: $f_{at}\left(\vec{R}_j + \vec{r}_g\right) = f_{at}(\vec{R}_j)$. The so-called shape factor (or form factor, or lattice amplitude), which depends only on the lattice type of the crystal, is defined as

$$S\left(\Delta\vec{k}\right) \equiv \sum_{\vec{r_g}}^{lattice} e^{-i\Delta\vec{k} \cdot \vec{r_g}} \tag{III.28}$$

The so-called structure factor, which depends only on the positions and types of atoms inside a unit cell, is defined as

$$\mathcal{F}\left(\Delta\vec{k}\right) \equiv \sum_{\vec{r_g}}^{basis} f_{at}\left(\vec{r_k}\right) e^{-i\Delta\vec{k} \cdot \vec{r_k}} \tag{III.29}$$

The decomposition of the scattered wave into a shape factor and a structure factor reflects the decomposition of a crystal into a lattice and a basis.

2.1.3 Laue Condition and Bragg Condition

If the incident electron beam is coherent, the scattered wave of different electrons have the same phase. The electromagnetic radiation at a given point in the space downstream beyond the lattice (usually the detector) is made up of contributions from each of these single electron scattered wave and if the relative phases of these contributions vary by 2π

or more, we may expect to find minima and maxima in the diffracted radiation. Such phase differences are caused by differences in the path lengths over which contributing electrons reach the detector (Figure III.3). The condition for constructive interference

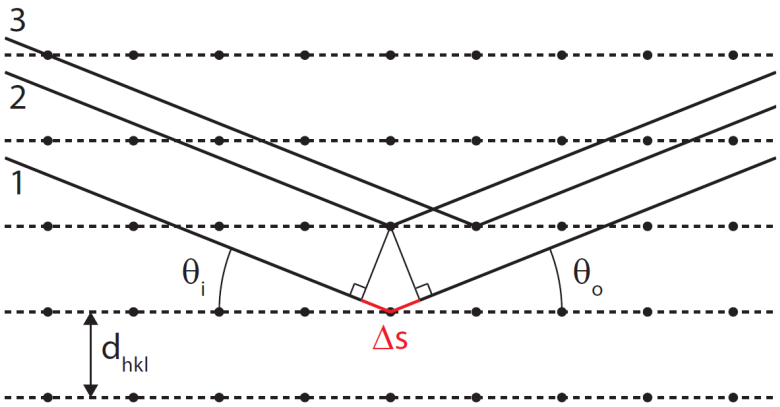

Figure III.3: Illustration of Bragg condition $\Delta s = \lambda$ for electrons scattering from lattice planes with spacing d_{hkl}. [23]

can be described in the reciprocal space, yielding the Laue condition, or in the real space, yielding the Bragg condition. Both conditions are thus principally the same, as explained in this section. The reciprocal lattice vectors $\vec{g}$ are defined by $e^{i\vec{g}\cdot\vec{r}_g} = 1$ and written as $\vec{g} = h\vec{a}_1^* + k\vec{a}_2^* + l\vec{a}_3^*$, where $\{h,\ k, l\} \in \mathbb{Z}$, and $\vec{a}_1^*$, $\vec{a}_2^*$, and $\vec{a}_3^*$ are the primitive vectors that span the reciprocal lattice. It can be shown that the reciprocal lattice vectors are normal to the lattice planes which are spaced a distance $dhkl = 2\pi/|\vec{g}|$ apart. Comparing the shape factor, as defined by Equation (III.28), with the definition of the reciprocal lattice, yields the Laue condition for constructive interference

$$\Delta\vec{k} = \vec{g} \tag{III.30}$$

This condition is visualized in Figure III.4 by the geometrical Ewald sphere construction: the tip of the incoming wave vector $\vec{k_0}$ is placed at a point of the reciprocal lattice. The center of the Ewald sphere is at the tail of $\vec{k_0}$ and the radius of the Ewald sphere equals $|\vec{k_0}| = 2\pi/\lambda$. Because for elastic scattering $|\vec{k_0}| = |\vec{k}| = k$ the tips of all possible scattered vectors $\vec{k}$ also lie on the Ewald sphere. In geometrical terms, the Laue condition states that constructive interference occurs when the Ewald sphere intersects a point of the reciprocal lattice. Because the wave vectors of the incoming and scattered wave have the same length, this condition is only fulfilled for certain scattering angles $2\theta_B$. This can also be considered in real space. Figure III.5a shows a plane wave incident on a surface at angle θ_i and scattered into an angle θ_s. The path difference between the two rays scattered at points O and P is $\Delta op = OP[cos\,(\theta_i) - cos(\theta_s)]$. Because the separation between O

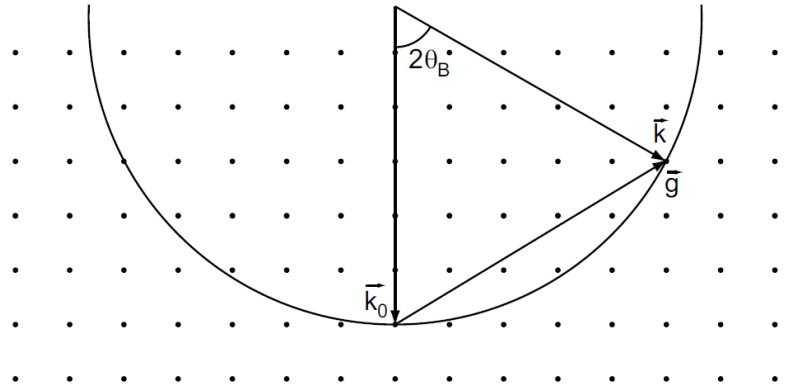

Figure III.4: Ewald sphere construction in the reciprocal space that shows for which reciprocal lattice points the Laue condition is fulfilled. [22]

and P is continuous, there will be as much destructive as constructive interference and no diffraction pattern will build up unless $\theta_i = \theta_s = \theta_b$. Figure III.5b shows a plane wave incident on a crystal lattice. Part of the plane wave is scattered by the upper plane of the crystal, while another part is scattered by the lower plane. From the Figure it can be derived geometrically that the path difference between these two scattered parts is $\Delta l = 2d\ sin(\theta_b)$. The scattered parts will interfere constructively if they are in phase, which is the case when the so-called Bragg condition is fulfilled

$$2dsin\left(\theta_b\right) = q\lambda \tag{III.31}$$

with θ_b the Bragg angle, λ the De Broglie wavelength of the electrons, d the lattice plane spacing, and $q \in \mathbb{Z}$. Using $d_{hkl} = 2\pi/\left|\vec{g}\right|$ and $\left|\Delta\vec{k}\right| = 2k\ sin\left(\theta_b\right) = \frac{4\pi}{\lambda} sin\left(\theta_b\right)$ it is straightforward to see that the Bragg condition and the Laue condition are equivalent.

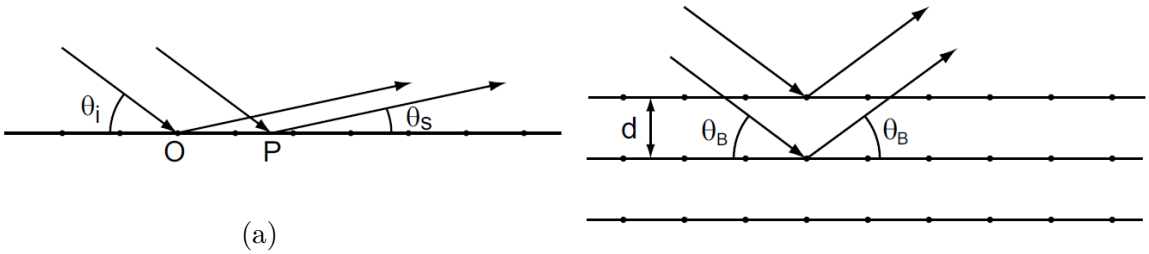

(a) (b)

Figure III.5: (a) Scattering of a plane wave with $\theta_i \neq \theta_s$. (b) Bragg angle θ_b for a plane wave scattering from different crystal planes. [22]

Chapter IV

Experimental Setup

ULTRAFAST phenomena, on picosecond and femtosecond time scales, can be investigated using pump-probe techniques, where a pump pulse excites the sample and triggers the ultrafast dynamics, and a probe pulse is used for monitoring the sample after an adjustable delay time (controlled through a delay line). [21] By repeatedly performing this pump-probe measurement as a function of the delay time, ultrafast dynamics can be observed. The time resolution of the experiment is limited by the time jitter, that is the stochastic uncertainty in measuring the delay between pump and probe. Ultrafast structural dynamics can be studied with atomic resolutions using ultrafast X-ray diffraction, Ultrafast Electron Diffraction (UED), and Ultrafast Electron Microscopy (UEM). A fundamental difference between using X-rays or electrons is the interaction with the sample: X-rays are scattered when they cause the atomic electrons to oscillate and re-radiate; electrons are scattered by Coulomb interactions when they penetrate the positively charged atomic core. The scattering cross section for 100 keV electrons is $10^4 - 10^5$ times larger than the cross section for X-rays [26]: electrons with mean free paths of 10 - 100 nm (for 100 keV) are therefore more suitable for studies of thin films (in transmission mode) or surfaces (in reflection mode), while X-rays can be used for studies of thicker samples.

1 Different Ultrafast Electron Diffraction Approaches

To obtain a high-quality diffraction pattern typically 10^6 electrons are required in low-emittance pulses. The space-charge forces in a pulse containing that number of electrons are still broadening the pulse to durations longer than 100 fs. Several approaches to circumvent this space-charge problem have been attempted. The obvious way to avoid the space-charge expansion is by using only a single electron per pulse. To limit the time necessary to build up a diffraction pattern the repetition frequency is raised to several

MHz [27]. In this approach, the temporal resolution is determined by the jitter of the arrival time of the individual electrons at the sample. Simulations show that using Radio Frequency (RF) acceleration fields, the individual electrons could arrive at the sample within a time-window of several fs (possibly even sub-fs) [28]. This single-electron approach, however, requires that the sample be reproducibly pumped and probed $\sim 10^6$ times to obtain a diffraction pattern of enough quality. A second approach is to extract ~ 1 fC electron bunches by femtosecond photoemission from a flat metal photocathode and to put the sample at a position as close as possible to the accelerator. In this way, there is simply less time for the Coulomb force to broaden the pulse. Space-charge effects limit the number of electrons to less than 10^4 per bunch for applications requiring high temporal resolution. A third method to overcome space-charge problems is to accelerate the bunch to relativistic speeds as quickly as possible. Close to the speed of light, the Coulomb repulsion is effectively suppressed by relativistic effects. Bunches of several hundred femtosecond durations, containing several pC, are routinely available from RF photoguns. However, energies in the MeV range pose their difficulties, including the very short De Broglie wavelength λ (~ 0.002Å at 5MeV), radiation damage to samples, reduced cross-section for elastic scattering, non-standard detectors and general expense of the technology. [22] [23]

The solution proposed by the researchers of the Department of Applied Physics of the Eindhoven University of Technology is to create an electron bunch longitudinally compressed through a "velocity bunching approach". [29] [30] An electron source for single-shot sub-100fs electron diffraction in the 100 keV range was developed, exploiting the velocity bunching effect using a cylindrical RF cavity resonating in the TM_{010} mode. We used this new source to monitor the diffraction peaks dynamics under the effect of the Free Electron Laser (FEL) pump.

2 Velocity Bunching Effect

Electrons of the same bunch, moving in an external oscillating electric field, are accelerated or decelerated depending on the phase of the external field. By properly tuning the phase, the front electrons are decelerated, and the back electrons are accelerated.This is the so-called velocity bunching effect. In this way, the longitudinal velocity-correlation in the bunch is reversed. The Coulomb interaction between electrons of the same bunch affects the compression. The shape of the electron bunch plays a fundamental role in the longitudinal compression. Because of its linear space-charge fields, a waterbag bunch can be compressed reversibly in the transverse and longitudinal direction with electromagnetic

lenses that have linear fields. In particular, the longitudinal expansion can be reversed using the time-dependent electric field of a cylindrical RF cavity resonating in the TM_{010} mode. The principle of using resonant RF cavities as longitudinal lenses for sub-relativistic UED is an established technique that is described in [29] [30].

The on-axis oscillating electric field inside the RF cavity is given by

$$\vec{E} \;=\; E\,(z)\,cos\,(\omega t \;+\; \varphi)\;\;\hat{z} \tag{IV.1}$$

with $E(z)$ the on-axis longitudinal electric field amplitude, ω the angular frequency and φ the RF phase. The change in longitudinal momentum Δp_z an electron acquires by traveling through an RF cavity is given by:

$$\Delta p_z \;\cong\; -\frac{eE_0 d_c}{v_z}\left(\frac{\omega\zeta}{v_z}\sin\left(\varphi\right) \;+\cos\left(\varphi\right)\right) \tag{IV.2}$$

with e the electron charge, $d_c = \int_{-\infty}^{\infty}\frac{E(z)}{E_0}\cos\left(\frac{\omega z}{v_z}\right)\,dz$ the effective cavity length, $E_0 \;= E(0)$ the electric field strength at the center of the cavity, v_z the average speed of the electron bunch and $\zeta \equiv \mathrm{z} - \mathrm{v_z t}$ the longitudinal electron coordinate with respect to the center of the bunch; φ is chosen as the RF phase at the moment the center of the electron bunch passes through the center of the cavity. [31] Equation (IV.2) shows that the average momentum change Δp_z of the electron pulse passing through the cavity is zero if the center of the bunch passes through the center of the cavity when the RF electric field goes through zero, i.e. $\varphi \;=\; \pm\,\pi/2$. Operating the cavity at a phase of $\varphi \;=\; \pi/2$ will result in bunch compression (Figure IV.1 bottom): the electrons in the front part of the bunch will be decelerated while the electrons in the back will be accelerated. Operating the cavity at $\varphi \;=\; -\,\pi/2$ will result in decompression (Figure IV.1 top), the electrons in the front part are accelerated and the ones in the back are decelerated.

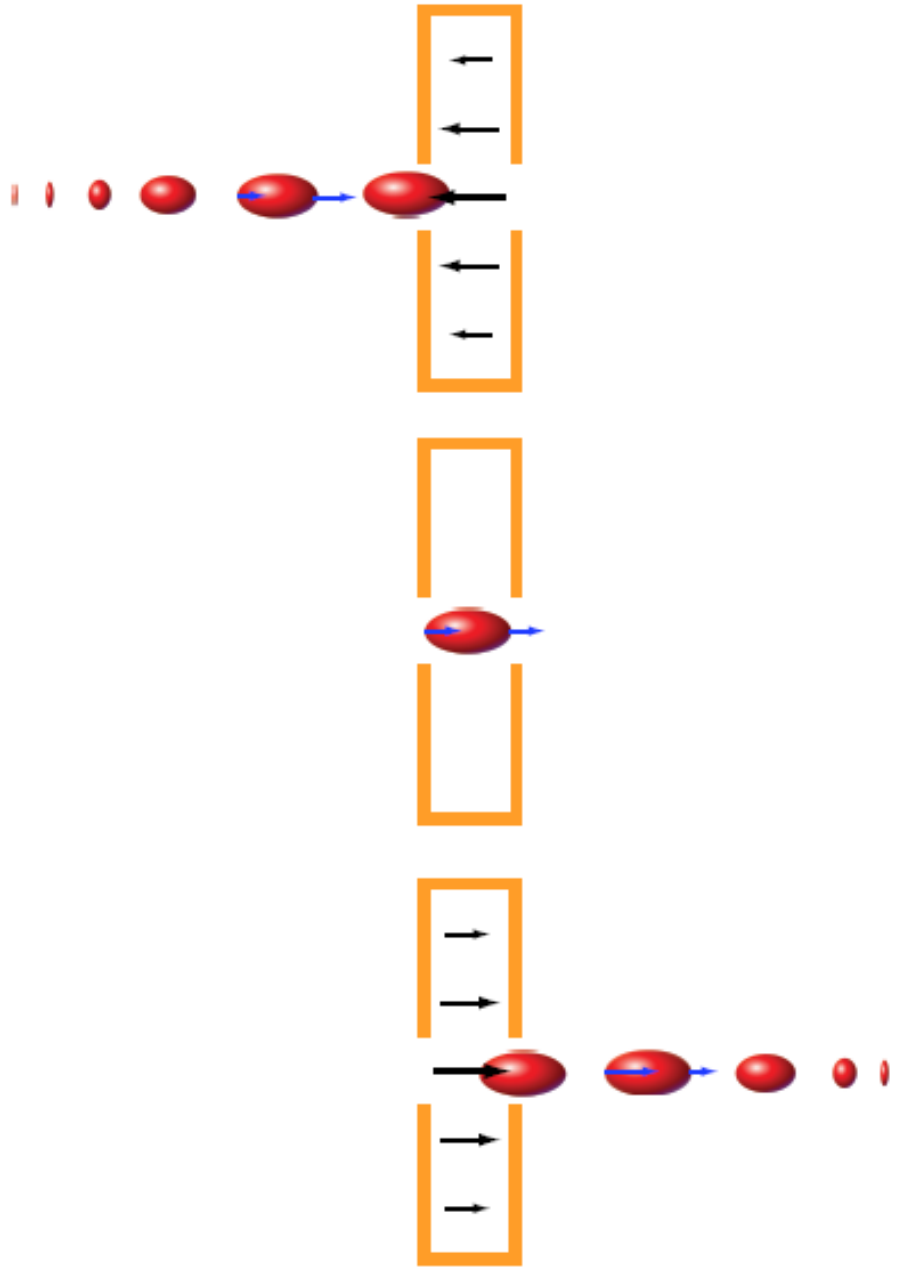

Figure IV.1: Principle of longitudinal compression of a (waterbag) electron bunch with a RF cavity. From top to bottom the same cavity is shown at increasing phase of a single RF cycle. (top) While traveling towards the cavity the bunch is expanding, as indicated by the blue velocity vectors. (Multiple bunches are shown for clarity.) The bunch enters the cavity when the force (black arrows) exerted by the RF field is decelerating. (center) While the bunch travels through the cavity the RF field goes through zero and will change sign. (bottom) As a result, electrons at the back of the bunch are accelerated, such that they will overtake the front electrons in the subsequent drift space. [22]

3 Electron Source

Figure IV.2 shows the electron source developed at the Eindhoven University. Electrons are generated from a copper photocathode (left in Figure IV.2) by a transversely shaped, ultrashort laser pulse and accelerated to an energy of 100 keV. After the anode, the first magnetic lens (high current solenoid cooled with water) is present. On the right of the lens, there is the window through which the laser pulses generate the waterbag electron bunches imping on the photocathode. Other two solenoidal magnetic lenses and a quadrupole are placed before and after the TM_{010} RF cavity in order to transversally focus the electron beam. In Figure IV.2 on the right, the connection to the EIS-TIMEX Chamber (flange CF63) is shown. The photocathode is bulk, high-purity (99.99%) OFHC copper

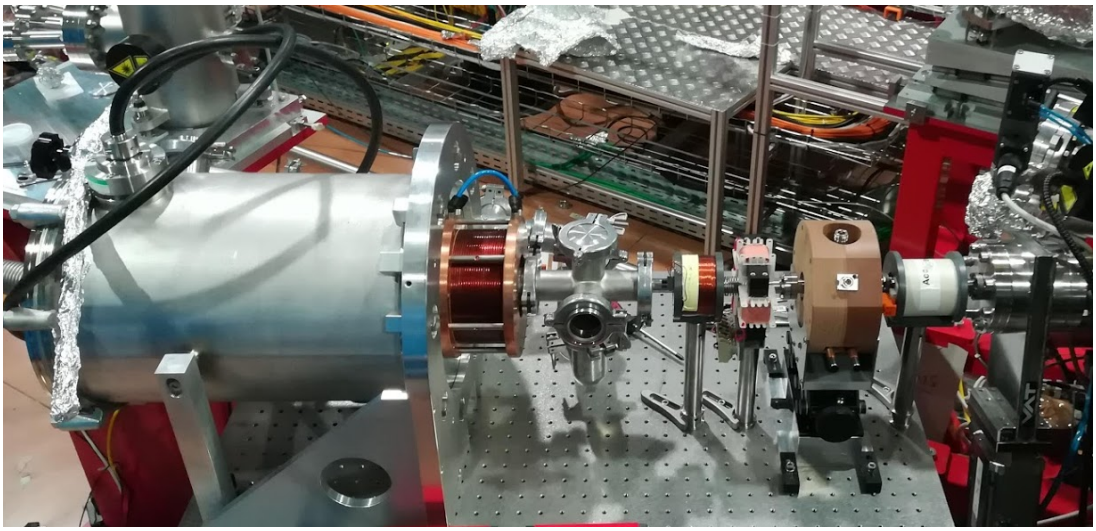

Figure IV.2: Electron source. From left to right: photocathode, high current solenoid, laser window, solenoid, quadrupole, RF cavity TM_{010}, solenoid, flange CF63 of EIS-TIMEX Chamber.

(Outokumpu, ASTM C10100). The photocathode is clamped in a holder (Figure IV.3). The cathode-holder is screwed onto the head of an aluminum cylinder, that is at a negative high-voltage (down to -100 kV). The outer cylinder, i.e., the stainless-steel vacuum vessel, is grounded and insulated from the inner conductor by a PolyEtherEtherKeton (PEEK) cone. The stainless-steel plate at the right side of the gun is the anode, which is grounded as it is connected to the outer cylinder of the gun. The photoemitted electrons are accelerated towards the anode and are leaving the gun through the hole. The hole is considerably larger than the spotsize of the beam to prevent bunch degradation during acceleration. By applying a DC voltage of 100 kV between the cathode and the anode an acceleration field of 10 MV/m is obtained, thus obtaining 100 keV electrons.

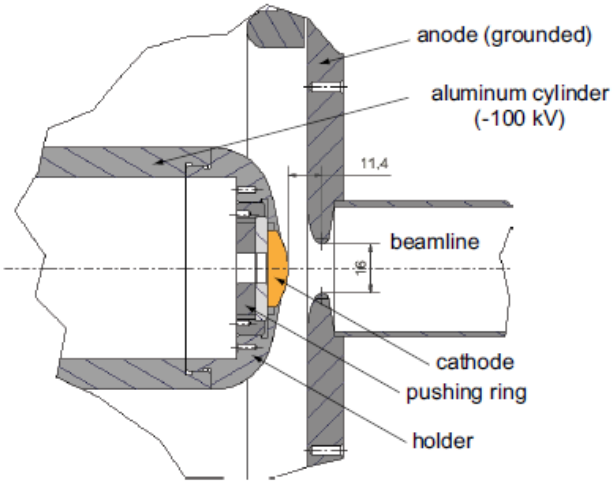

Figure IV.3: Scheme of the photocathode of the electron source. [29]

A Radio Frequency (RF) cavity is a metallic chamber that contains a space and time dependent electromagnetic field. Its primary purpose is to accelerate charged particles. To prepare an RF cavity to accelerate particles, an RF power generator supplies an electromagnetic field. The RF cavity is modelled to a specific size and shape so that electromagnetic waves become resonant and build up inside the cavity. In our case, the cavity is made out of two OFHC copper (Outokumpu, ASTM C101000) half cells that are brazed to each other to make the cavity vacuum compatible. The designed resonant frequency of the RF cavity, used to compress the electron bunch, is 2.9985 GHz.

4 Combining EIS-TIMEX and the Electron Source

In this work, we succeeded in combining the electron source described in the previous section with the FERMI beamline EIS-TIMEX. The pioneering setup achieved open unprecedented class of experiment to generate and investigate extreme states of matter. In this section is described how we reach this setup, which we consider a result by itself. The scheme of the experimental setup is shown in Figure IV.7.

We used the Seed Laser User (SLU) pulse ($\lambda = 260$nm) to generate the electron bunch on the copper bulk photocathode of the electron gun via photoemission. This peculiar approach allowed us to have an uncertainty on the arrival times between pump and probe smaller than 10 fs. Indeed, the SLU pulse is obtained by splitting the Seed Laser which triggers the Extreme Ultraviolet (EUV) FEL radiation emission at FERMI. As described previously, the RF cavity is designed to be driven by a signal with a frequency of 2.9979

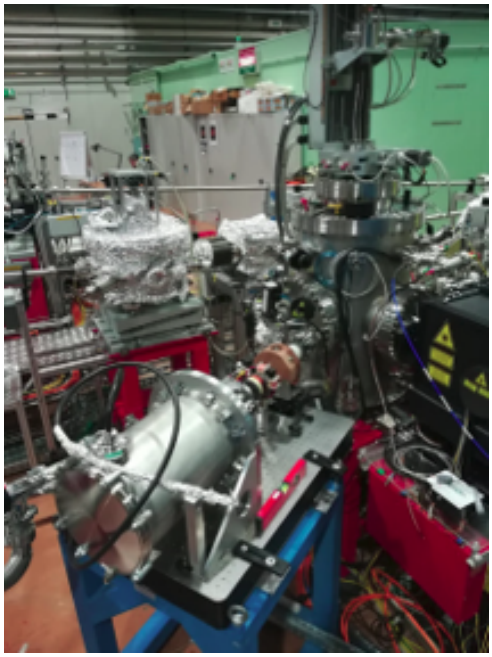

Figure IV.4: View of the setup in the experimental hall of FERMI. At the bottom, there is the electron source, which is connected to the EIS-TIMEX Chamber (middle). The black box on the right contains the setup of the "seed laser for users" (SLU) used to excite the gun photocathode.

GHz. The FERMI LINAC, which accelerates in a single stage the electron bunch that produces the FEL radiation, has a frequency of 2.998 GHz. Therefore, we used an optical fiber (hundreds meter long) in order to use the LINAC frequency to drive the RF cavity in the gun. This signal has a short-term stability of few femtoseconds. However, the long-term stability was affected by thermal drift due to the length of the cable. This uncertainty is not critical to perform velocity bunching in the RF cavity, because it depends only on the optical jitter between FEL and the electron probe. The RF cavity was always kept at 18°C by a specific chiller. In fact, the thermal expansion varies the dimension of the cavity, which is strictly related to the resonance frequency. The electrons are accelerated by a 100kV bias, reaching an energy of 100keV at the end of the gun, corresponding to photons with a wavelength of 0.037 Å. This fact highlights the suitability of the electron source to perform UED with EUV FEL pump. Indeed, the penetration depth of 100keV electron bunches on the samples is comparable to the photon one. In the experiment the photon wavelength was set at 25nm.

Before the photoemission, the SLU was equipped with a delay line to tune the delay time between pump and probe. Tuning the delay time, it is possible to resolve in time the ultrafast dynamics generated by the pump. The view of the setup in the experimental hall at FERMI is shown in Figure IV.4.

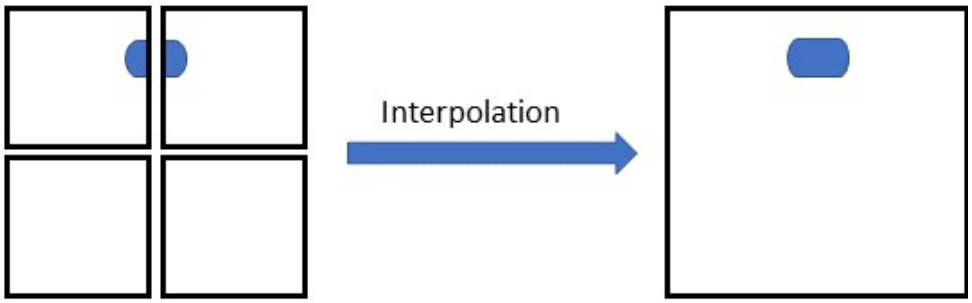

Figure IV.5: Scheme of the TimePix detector. On the left, the structure of the detector is sketched. A diffraction peak (blue) that is registered in the cross-shaped region after the interpolation process would give a diffraction image as the one shown on the left.

Working in transmission, in the opposite side of the EIS-TIMEX chamber with respect to the gun the detector is placed. For detection, we used a TimePix four quadrant electron detector. [32] The detector is built up by four components so that a cross appears in the middle of the diffraction image (Figure IV.5). The data in those regions of the detector are interpolated via a MATLAB code. Above the detector, a long-distance microscope (telemicroscope) is placed for fine alignment and rough beam profile measurements. The main piece of equipment of the EIS-TIMEX end-station is the 5-axis motorized sample manipulator stage working in the main EIS-TIMEX chamber. The manipulator can operate for single-shot measurements and allows accurate sample alignment in the interaction region with pump and probe pulses. In the middle of the chamber, the sample holder is placed (Figure IV.6b). The incident angle between pump and probe was 20°. The experiment was conducted in transmission. The FEL radiation enters the chamber after passing through the Photon Analysis Delivery and Reduction System (PADReS). To align and focus the pump on the sample holder, an ellipsoidal mirror is used. We decided to work with the tenth harmonics of the seed Therefore, the pump wavelength was 25 nm. In the photon transport, filters can be placed. Either the electron source and the EIS-TIMEX chamber were kept under vacuum, 10^{-6} mbar and 10^{-8} mbar, respectively. To monitor the vacuum, we used Penning and Pirani gauges. The out part of the EIS-TIMEX chamber is shown in Figure IV.6a.

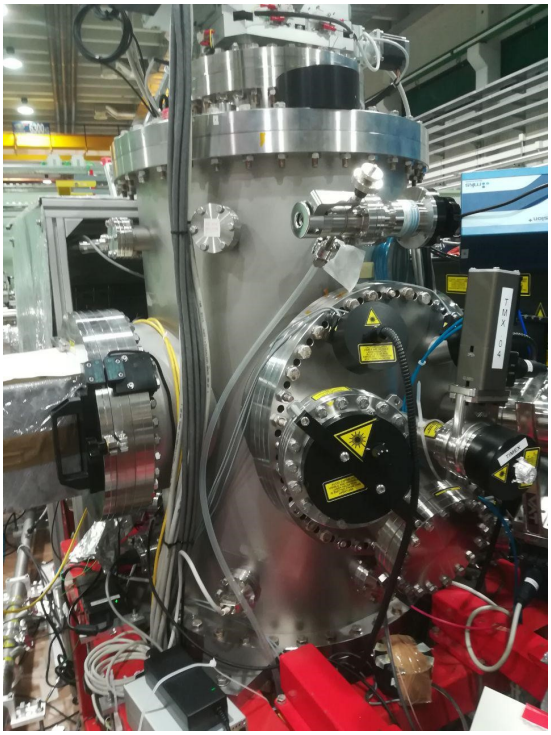

(a)

(b)

Figure IV.6: EIS-TIMEX Chamber (a) and sample holder (b). In the first image, the TimePix detector, on the left, is connected to the chamber. In the image on the right, the samples glued on the sample holder with carbon tape are shown. On the top there are two gold foil 20 nm thick. The diamond membranes deposited on silicon wafer with window are in the middle. The circular-shaped samples are copper TEM grid used in the overlapping of the pump and the probe on the sample plane. Above the diamond sample, the monocrystalline gold sample is placed.

5 Upgrades

As mentioned before, it was the first time that a FEL beamline was combined with an electron source to perform UED and investigate sub-ps dynamics. Therefore, several components of the experimental setup can be improved. As shown in Figure V.3 the area of the pump was smaller than the area of the probe. Moreover, when the electron beam was focused on the sample, it was defocused on the detector. Defocusing on the sample would result in a bigger spot size on the sample plane. This condition must be avoided to probe only the excited region. On the other hand, defocusing on the detector affects the resolution of the diffraction pattern. The size of the TimexPix detector was about $25x25mm^2$ at a distance from the sample of about 35 cm. So, the angle of diffraction allowed from the setup of the order of few degrees. In our working conditions,

we decided to focus the beam on the sample plane, thus getting a worse focus on the detector. This undesired condition can be mitigated by adding further magnetic lenses to focus the beam on both the sample and the detector plane. Our setup doesn't provide any measurement of the bunch compression. We estimated the bunch length through numerical calculations. However, it could be interesting studying how the bunch pulse duration affects the measurement. For this measurement, the electron source could be combined with a streak camera as described in [33] [22].

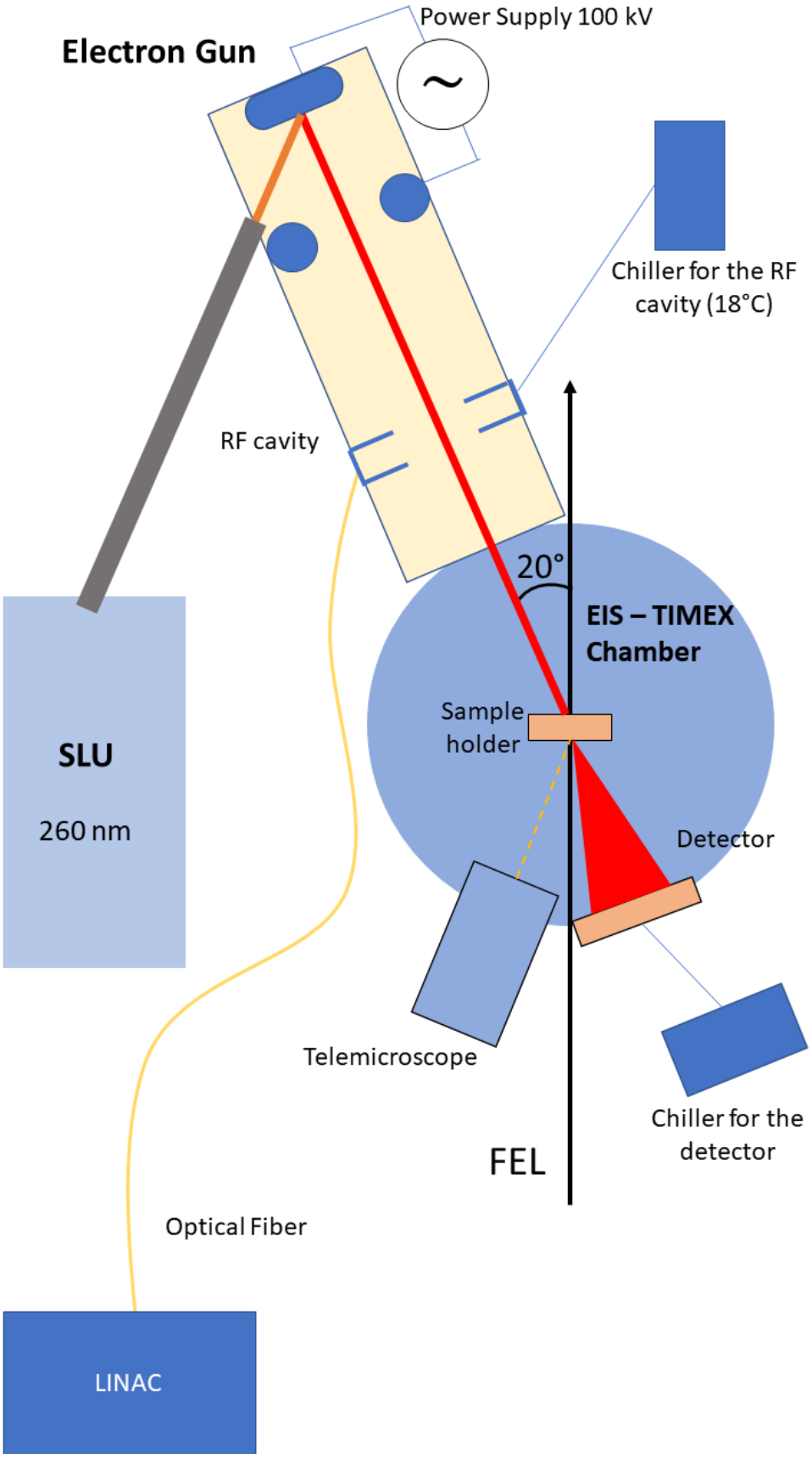

Figure IV.7: Scheme of the experimental setup.

Chapter V

Results

In this chapter, the results of the first time resolved electron diffraction experiment with Free Electron Laser (FEL) pump will be presented. The pioneering setup, described in Chapter IV, was used to investigate the ultrafast melting of both single crystal and polycrystalline gold, and single crystal diamond. The measurements were carried out at the EIS–TIMEX beam line of the FERMI facility in Trieste employing a pump-probe approach to generate and probe the melting of the samples. The data analysis is still ongoing at the time of writing and E. Principi is recognized as the principal investigator on this topic. The experiments were performed in the framework of a collaboration between the TIMEX group and the Department of Applied Physics of the Eindhoven University of Technology. The method employed to synchronize the FEL pulse and the compressed electron bunch on a copper TEM grid is initially presented; this is a crucial step to conduct the experiment. After a brief description of the samples under investigation, the time-resolved evolution of the diffraction peak of monocrystalline diamond and gold is reported. The last section describes the data obtained with the same setup on a polycrystalline gold thin film of 20 nm thickness.

It is important to highlight that this is the first time that this class of measurements was carried out at FERMI. Neither the synchronization between FEL-pump and nonrelativistic 100 keV electron-probe with fs time precision nor the experimental method were granted to succeed. It is a significant result that the experimental setup proved successful because it opens a new unprecedented class of experiments that allow to access transient states of matter. Being a pilot experiment, it can be improved with several upgrades. Chapter IV, Section 5 describes possible improvements in the experimental set up which could increase the resolution and the amount and the quality of the information obtainable.

1 Space Charge Effect and Compression of the Electron Bunch

The velocity bunching approach (Chapter IV, Section 2) with an Radio Frequency (RF) cavity allows sub-ps compression of the electron bunch generated by the electron gun. To do so, it is mandatory to synchronize the phase of the RF cavity field and the Seed Laser User (SLU). Impinging on the copper cathode of the electron gun, the SLU generates the electron bunch, which is then accelerated to an energy of 100 keV. As described in Chapter II, the SLU pulse is obtained splitting the seed laser which triggers the Extreme Ultraviolet (EUV) FEL radiation emission at FERMI. This approach allows reducing the uncertainty in the delay between pump and probe (the so-called "time jitter") below 10 fs in the EIS-TIMEX end-station. We were able to synchronize the SLU and the RF cavity. The signal that defines the frequency of the Linear Accelerator (LINAC) S-band (Chapter II, Section 5.1) in the generation of the FEL radiation was used as driven frequency of the RF cavity. This setup allows us to obtain a temporal jitter between the electron bunch (probe) and the FEL radiation (pump) of about 10 fs and to finely adjust the phase of the RF cavity. The time interval between pump and probe ("delay") pulses can be tuned by changing the optical path of the SLU, before it generates the electron probe.

Once chosen the RF signal to drive the cavity (Chapter IV, Section 4), the RF cavity TM_{010} parameters are the amplitude and the phase of the electric field. To understand the right values for the amplitude and the phase, we tuned the phase keeping the amplitude constant. The RF power, which is related to the amplitude of the electric field in the cavity, and the phase cause the compression of the bunch, according to the velocity bunching effect [31]. The values of these two parameters must be set to avoid two opposite unwanted conditions. If the RF power is greater than the velocity bunching condition it causes the over-bunching effect. In over-bunching, electrons in front of the bunch are decelerated and the electrons behind are accelerated Figure IV.1. So that, after interacting with the oscillating electric field, an electron that was in the front of the bunch is in the tail, and viceversa. This configuration results in a less compressed bunch. If the phase is set wrong the bunch is less compress, which increases the longitudinal dimension of the bunch causing the decrease of the temporal resolution of the probe.

Initially, we focused the electron beam on the sample with the RF cavity off. After reaching the smallest spot size on the sample, using only the solenoids, we switch on the RF cavity. We fixed a reference power value to investigate the compression of the bunch

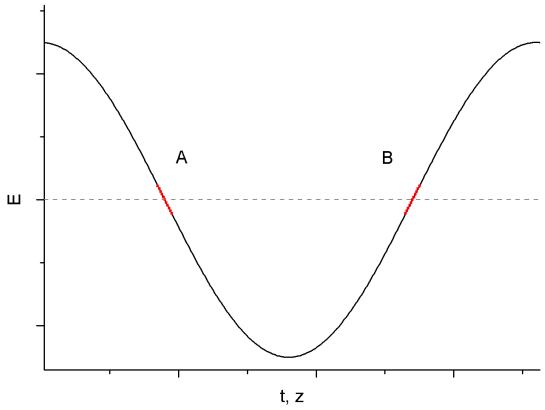

Figure V.1: Electric filed in the RF cavity. In A the velocity bunching effect takes place. The dashed line indicates zero.

at different phase values. During the phase scan, the solenoid focuses more if the electron average energy is lowered by the cavity, it focuses less otherwise. Being in the best focus (on the sample plane) configuration with the RF cavity off, ensure that the change in energy will be revealed as an increase of the spot size of the beam. There are two phase values for which the average energy is equal to the energy without the RF cavity. These values are minima. When the bunch is compressed, the space charge effects dominate the spot dimension on the sample. Figure 1 shows the oscillating electric field inside the cavity. In point A and B the average energy is the same, but the field in the cavity has a different gradient so that in one case the tail of the bunch is accelerated and the head is braking (compressed bunch), in the other case the bunch is stretched and dilute. If the bunch is compressed, the charge density is greater, which results in a stronger space charge effect. This means that the phase value for the velocity bunching corresponding to the minimum (A or B) is the one that causes a bigger spot size on the sample. Once estimated the phase value, the RF power was set equal to 25 W.

2 Temporal and Spatial Overlapping of FEL-pump and Compressed Electron-probe

After setting the values for RF cavity and phase and focusing the 100 keV electron beam, we overlapped the FEL pulse and the electron bunch both transversally (spatially) and longitudinally (temporarily). The spatial overlapping is also necessary to measure the temporal distance between the two beams. We used a TEM grid of copper for this purpose.

When the FEL radiation impinges on the TEM grid, after few ps the plasma is formed. The FEL radiation creates a hole in the sample. We used the hole to overlap the electron bunch (probe). The best overlapping corresponds to the highest peak intensity registered by the detector. Figure V.2 shows the effect of the FEL radiation on the TEM grid. The

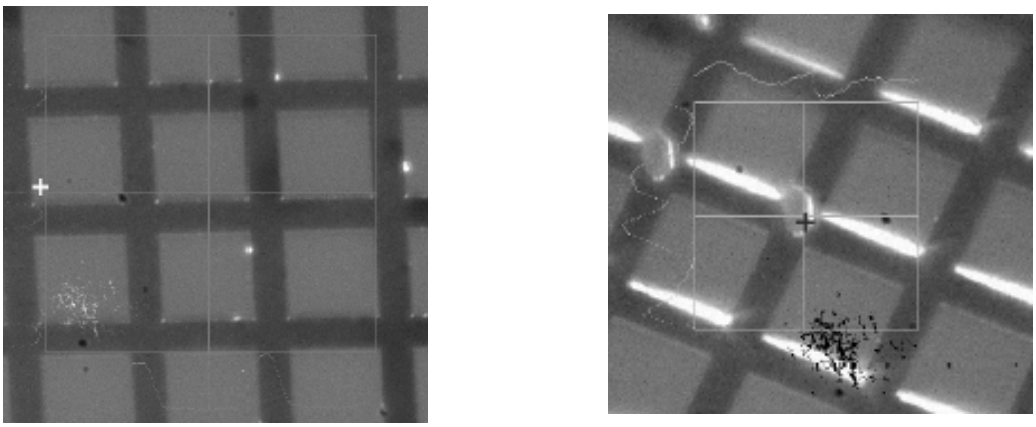

(a) (b)

Figure V.2: Copper TEM grid before (a) and after (b) FEL radiation exposure.

best working condition in pump-probe experiments is that the spot sizes of both pump and probe are comparable. Ideally the pumped area should be greater than the probed area. This is not the case because even if the bunch is compressed, the space charge effect set a limit in terms of the transverse dimension of the beam. Being chargeless, photons of the FEL radiation are more compressed. This means that the effect that we were detecting was an average between the unexcited sample region (out of the FEL spot size but hit by the electron beam) and the effectively excited sample region. To decrease this discrepancy, we moved the focus of the FEL a bit beyond the sample position. We couldn't move the focus further, otherwise, the FEL fluence wouldn't be enough to generate the plasma. Moreover, we decided to not compress the electron bunch as much as we could, because it will result in a loss of resolution on the detector caused by the space charge effect, which would have spread the electrons after crossing the sample. Figure V.3 shows a typical spot of the beams. Once the beams were spatially overlapped, we measure the time zero (t_0), which correspond at the delay position of the delay line that cause the beams to simultaneously imping on the sample. As first rough overlapping in time, we used an antenna (screened SMA cable) to measure the temporal difference between the arrivals of both pump and probe on the sample plane. The antenna was attached to the sample holder. We measured with an oscilloscope the electrical pulses associated with the pump and the probe impinging on the antenna, reaching a temporal uncertainty of the order of $\sim 20ps$. After that, we sent the beams on to the TEM copper grid. When the electron

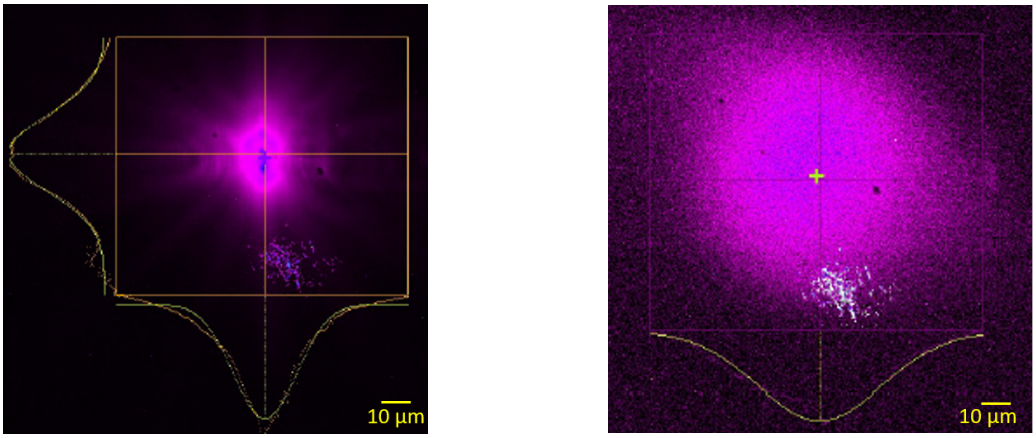

(a) (b)

Figure V.3: Spot size of the FEL radiation (a) and the electron beam (b) on a YAG screen.

bunch passes the grid before the arrival of the pump pulse ($t < 0$), no plasma effect is visible; when the electron bunch passed after the pump pulse ($t > 0$) the occurrence of the plasma alters the primary beam transversal distribution and can be detected in the electron detector. In Figure V.4 the relative intensity variation of the direct beam on the detector is plotted as a function of the delay between the pump and probe beams. The delay has been adjusted based on the estimated position of $t = 0$.

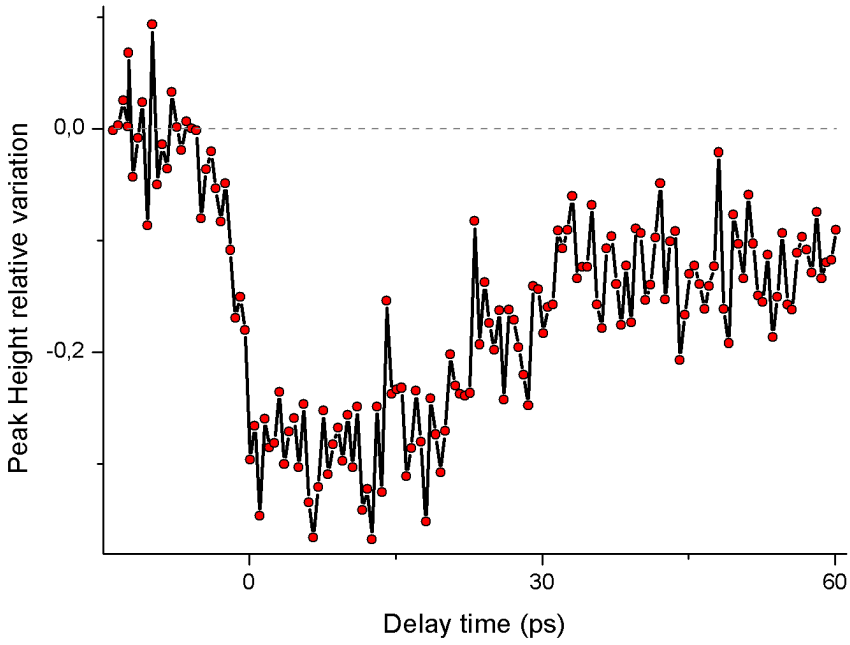

Figure V.4: Delay scan of the electron primary beam intensity after interaction with a laser-excited TEM grid for getting the "time zero" between pump and probe.

3 Samples

Carbon (C) is ubiquitous in the Universe and represents the constituent element of every life form present on the earth. It exhibits a pronounced chemical flexibility that gives rise to its exceptional polymorphism. The comprehension of polymorphism in carbon and its origin at the electronic level is an essential step to successfully predict the phase diagram of covalent substances and finally understand the intriguing anomalies that they typically exhibit. However, a detailed experimental investigation of the structural properties of the condensed phases of C is limited to the graphite and diamond forms available under ambient conditions. Access to the liquid phase under stationary conditions is extremely complex as it requires an experimental setup capable to heat carbon up to about $5000K$ avoiding sample sublimation at moderate pressures as well as collapse of the pressurization device. Moreover, a thorough exploration of the p-T phase diagram including other solid polymorphs of carbon, demands to further extend the temperature range and operate in the Mbar pressure regime. A valid solution to those issues is offered by sub-ps EUV FEL pumps capable to induce volumetric isochoric heating and pressurization on optically opaque solid samples. Ultrafast heating can drive a micrometric region of a condensed carbon specimen to extreme conditions of pressure and temperature. Diamond is a solid

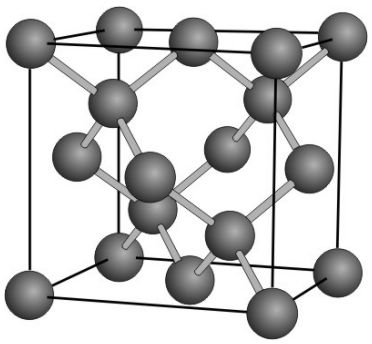

Figure V.5: Diamond unit cell

form of pure carbon with its atoms arranged in a crystal. In diamond structure the chemical bonds are sp^3 and the atoms form tetrahedra with each bound to four nearest neighbours. Tetrahedra are rigid, the bonds are strong, and of all known substances diamond has the greatest number of atoms per unit volume, which is the reason why it is both the hardest and the least compressible material. The crystal structure of the unit cell of the diamond is shown in Figure V.5. A diamond cubic lattice can be thought as two interpenetrating face-centred cubic (fcc) lattice with one displaced by 1/4 of the diagonal along the cubic cell.

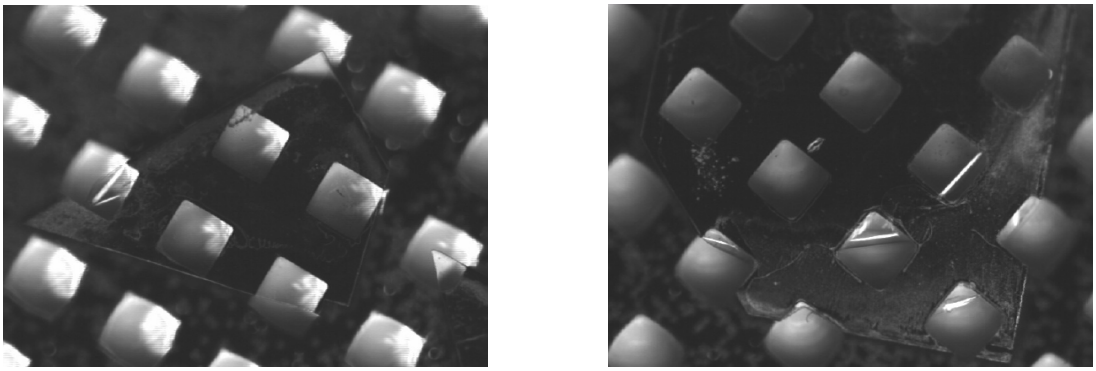

Figure V.6: Diamond membranes deposited on a silicon wafer. The images were obtained with an optical microscope.

Being our setup based on the transmission of the electron beam, after the interaction with the atoms forming the diamond lattice, we must have the thickest diamond sample as possible. Usually there is no bottom-up process able to reach the thickness we demand. This is because diamond cannot be normally grown heteroepitaxially. However, the MCN (University of Melbourne) succeeded in growing 50 nm thick diamond single crystal samples, with the following non-standard procedure. They started with their standard diamond membrane around 200µm up to 3mm in lateral dimensions and around 300 nm thick. These membranes were deposited on a silicon wafer with windows in it. The membranes were etched down to 50 nm. Figure V.6 show the diamond samples at the optical microscope.

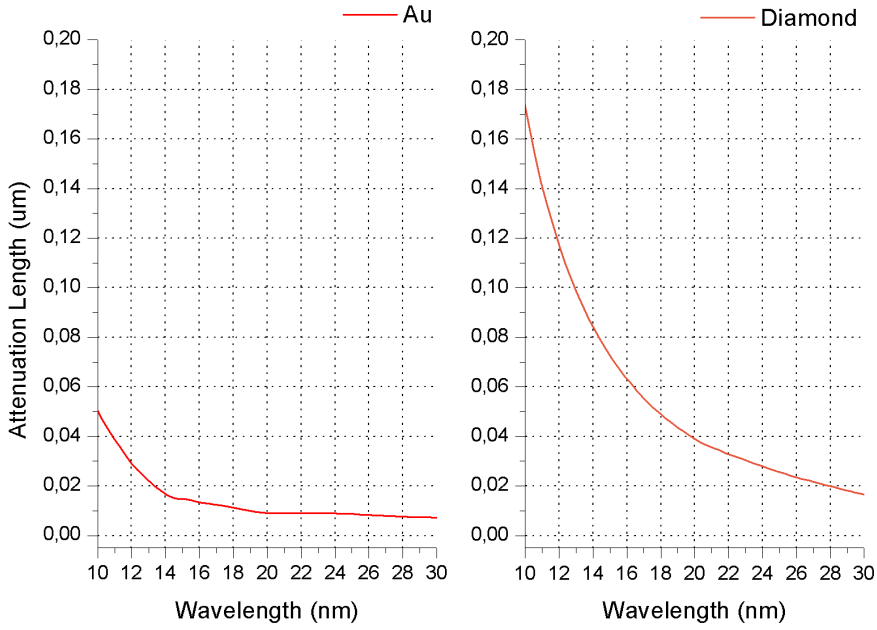

Figure V.7: Attenuation length of gold (left) and diamond (right) in the EUV spectral region.

We have also investigated two different gold sample. The reason is that the attenuation length of diamond and gold are quite comparable (Figure V.7), allowing us to investigate the gold samples without varying any part of our set up. We investigate a single crystal gold sample and a polycrystalline 20nm thick gold foil. Figure V.9 shows the ultrafast electron diffraction image of both the polycrystalline and monocrystalline samples. The images are obtained by averaging several single shot acquisitions. Gold (Au) crystalline structure is fcc, with an atom of gold at each corner and sitting in the middle of each face, as shown in Figure V.8. Gold is relatively soft, but it is also very malleable. This is another reason why it was investigated during the experiment.

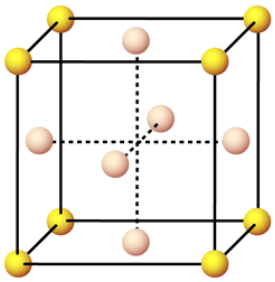

Figure V.8: Gold unit cell.

4 UED Results

After the characterization of both pump (FEL) and probe (electrons), we set our working conditions. We set the RF power of the electron gun at 25 W. We optimized the phase of the radiofrequency cavity to be in the configuration described in Chapter IV. If we compressed further the electron beam on the sample, we would have lost resolution on the detector. On the other hand, reaching the best resolution on the detector would have been possible only increasing the spot size of the beam onto the sample. In our working conditions, the ratio between the area of the pump spot and the area of the probe was 38%. Only about 38% of the electrons of the probe were sensitive to the hot sample region, exposed to the FEL beam. Using the tenth harmonic of the seed laser, the wavelength of the FEL radiation was 26nm. The energy of the source before the filters was 85 µJ. We used two filters of aluminum 200nm thick for the monocrystalline samples and four filters of aluminum 200nm thick for the polycrystalline one. I estimated the energy of the pump on the sample to be 38µJ and 17 µJ, with two and four aluminum filters respectively. By knowing the spot size of the FEL radiation, I calculate the energy density in the samples. In this calculation, I assume the spot as an ideal circle with radius equal to the peak

width (35 µm). Moreover, considering the gaussian distribution of the photon on the sample, I estimated that only 68% of the photons reach the sample in a spot of radius equal to 35µm. The energy densities are reported in Table V.1. The last column shows the bonding energies for gold and diamond, respectively. The deposited energy density has to be greater than bonding energy to activate the melting process in the sample. The bonding energies reported refer to a bulk material. [34] Having samples sub-100 nm thick allows us to consider those values as an upper limit. In fact, the average energy per atom is lower, because the atoms at the surface have less bond. Moreover, in our case, the samples were driven out of equilibrium, so that classical Thermodynamic arguments and their results are not applicable properly.

Sample	Deposited energy density (eV/atom)	Bonding energy (eV/atom)
Gold Polycrystal	36.6	2.99
Gold Single Crystal	16.5	2.99
Diamond Single Crystal	4	7.4

Table V.1: Energy density value for the different samples investigate. The last column shows the bonding energies for the samples.

Figure V.9 shows typical diffraction patterns of each samples investigated. The cross that appears in each image is because the detector is composed by four units. The intensity values of these pixels are interpolated, using the neighbours pixels (Figure IV.5). To detect the dynamic of the diffraction peak (ring in case of polycrystalline sample), we acquired diffraction images with and without pump (from now on called "pumped" and "preshot", respectively), keeping fixed the delay time between pump and probe. The data acquired without the pump were used during the analysis to normalize the data with the pump on.

It must be highlighted that this pump-probe technique is irreversible. Once a measurement has been carried out, the sample presents a hole in the probed region. To increase the signal to noise ratio, I averaged several single shot images (without mixing preshot and pumped). This procedure is strongly dependent on the number of diffractive images acquired per delay time and on the sample. If the sample is not homogeneous this approach can't be performed. During the data analysis, I assumed that the gold samples were reasonably homogeneous. It can't be assumed the same for the diamond sample. We investigated six different diamond samples, all single crystals, but with different orientation.

Moreover, the diamond windows deposited above the silicon wafer were only 30. So that the statistics of this sample was very small.

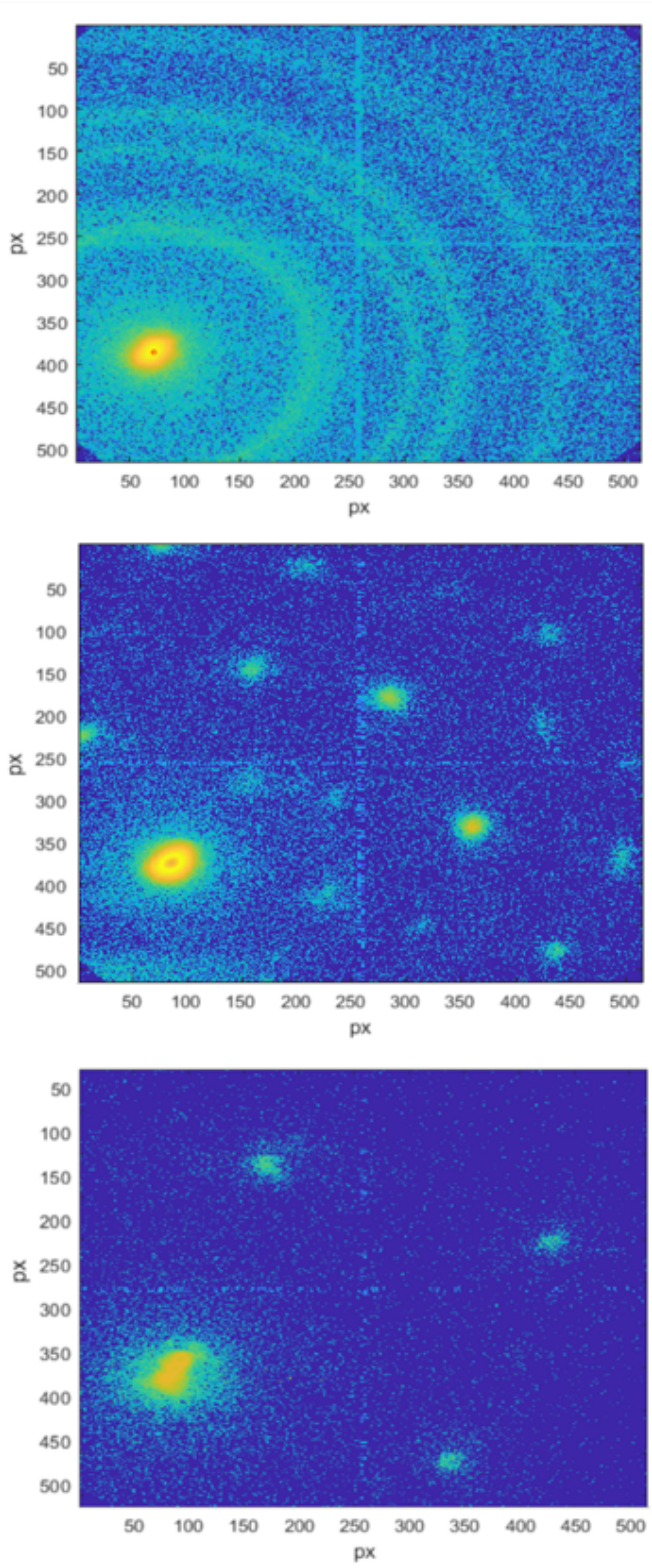

Figure V.9: Diffraction images of polycrystalline gold (a), gold single crystal (b) and diamond single crystal (c).

Keeping in mind that the experiment goal is a proof of principles, I decided to consider all the diffraction peaks of the diamond samples as one peak. This strategy has two consequences: increase the signal to noise ratio allowing fitting procedure for further analysis, lose information about the individual behaviour of each peak. I choose this procedure in order to understand if we were sensible to the diamond global melting.

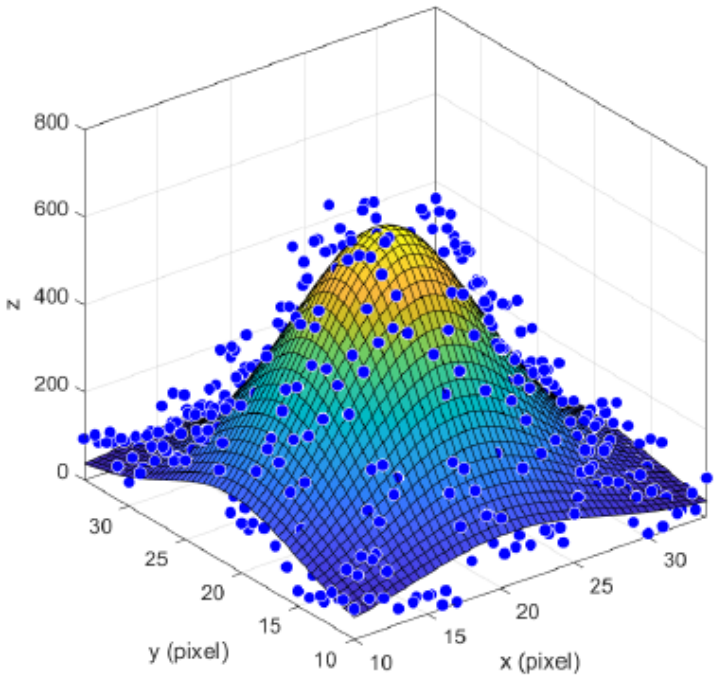

Figure V.10: 2D Pseudo Voigt fit.

Even with this method, I had to filter the data with a Fourier filter, so that my MATLAB code could perform a 2D-fit of the peak. I decided to use a Pseudo – Voigt function to fit the peak, which is a linear combination between a gaussian and a Lorentzian curve. The reason for this choice can be found in the fact that this curve adapts better to the peak height w.r.t to a usual gaussian [35]. The formula I used is:

$$I_{peak}\left[\left(\frac{\eta}{1+\left(\frac{x-x_0}{\delta_x}\right)^2+\left(\frac{y-y_0}{\delta_y}\right)^2}\right)+(1+\eta)\,e^{-\log(2)\left(\left(\frac{x-x_0}{\delta_x}\right)^2+\left(\frac{y-y_0}{\delta_y}\right)^2\right)}\right] \quad \text{(V.1)}$$

where η is the linear coefficient ranging from 0 to 1, x_0 and y_0 are the coordinates of the maximum of the peak, δ_x and $\delta_y$are the Full Width at Half Maximum (FWHM) of the curve in x and y direction respectively. For each delay time, I fit both preshot and pumped data (Figure V.10). The final result, reported in Figure V.11, consists on the relative change of intensity between preshot and pumped. The error bars were estimated starting from the relative error of the detector and then multiplying this value with the intensity

data. We decided to apply this method to have reasonable error bars. The error obtained as output of the fit were unreasonably small.

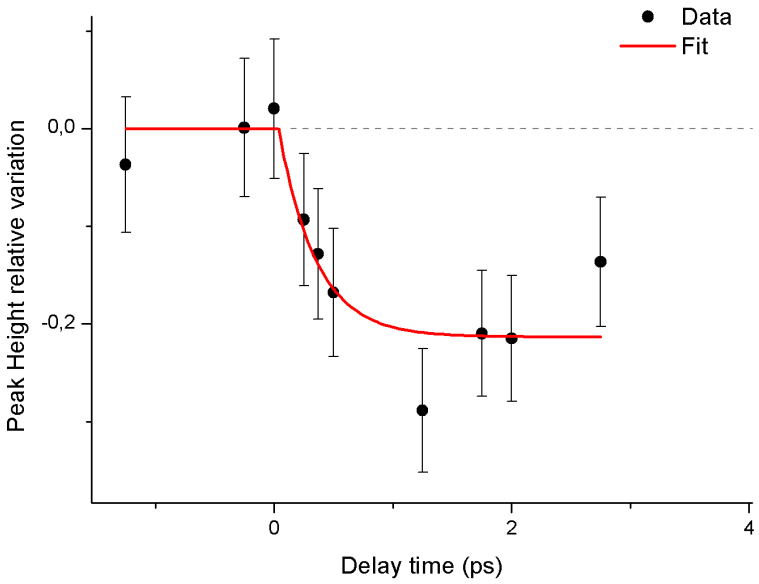

Figure V.11: Peak height relative variation for the diamond sample.

I used the following formula to calculate the relative intensities from the fit parameters:

$$\frac{I_{peak}^{pumped} - I_{peak}^{preshot}}{I_{peak}^{preshot}} \tag{V.2}$$

As the Figure V.11 shows, at t $<$ 0 the probe arrives on the sample before the pump, so that ideally $I_{peak}^{pumped} = I_{peak}^{preshot}$. At t $>$ 0 all the points are below zero. This indicates that the melting is taking place. The time of melting is of the order of 1 ps. In fact, after 1 ps the Bragg peak height is 20% less w.r.t negative times. This is in agreement with the melting of the excited region of the sample (38% of the probe). By considering all the Braggs peak as one, I didn't analyse the FWHMs. In fact, each peak is oriented with respect to the direct beam peak. This means that only in the ideal case in which the peaks are circular in the XY plane, the procedure used to increase the statistics doesn't affect the FWHMs results. This is not the case for the heights, because the ROIs were summed up centred on the peak barycentre.

I applied the same analysis to the data acquired for the monocrystalline gold sample. Having enough samples, in this case, I consider only the peak (111) without averaging all the peaks together. In this case, I analysed also the FWHMs. In Figure V.12 is reported the graph obtained for the dynamic of the Bragg peak. In this case, we acquired 20 preshot

and 20 pumped images per delay position. With this amount of data, the plateau at $t < 0$ is well defined. However, the graph shows that added to the melting dynamics of the peak there is a damped periodic trend, which starts at $t = 0$. These oscillations have a period of 8ps. The same trend, but shifted of half period, is present also in the FWHM evolution in time. Oscillations of this kind could be ascribed to the activation of either a compression wave moving at the velocity of sound in the sample bulk or a coherent phonon. [36] [37] In literature, the response of materials to intense visible fs-laser pulses sometimes exhibits oscillations of the lattice spacing with similar period (0.1-0.2 THz). That effect is often associated with the presence of a compression wave traveling through the sample and the period of the oscillation is given by both the sound velocity in the sample and sample thickness. However, in this experiment, the periodic change in both the peak height and width seems not to be associated with a fluctuation of the lattice spacings. Indeed, the peaks position doesn't exhibit a clear dynamics in time and the fluctuations are within the experimental uncertainty. Therefore, the nature of the observed oscillations is still unclear. Even in this case, the lattice heating time is $\sim 1ps$.

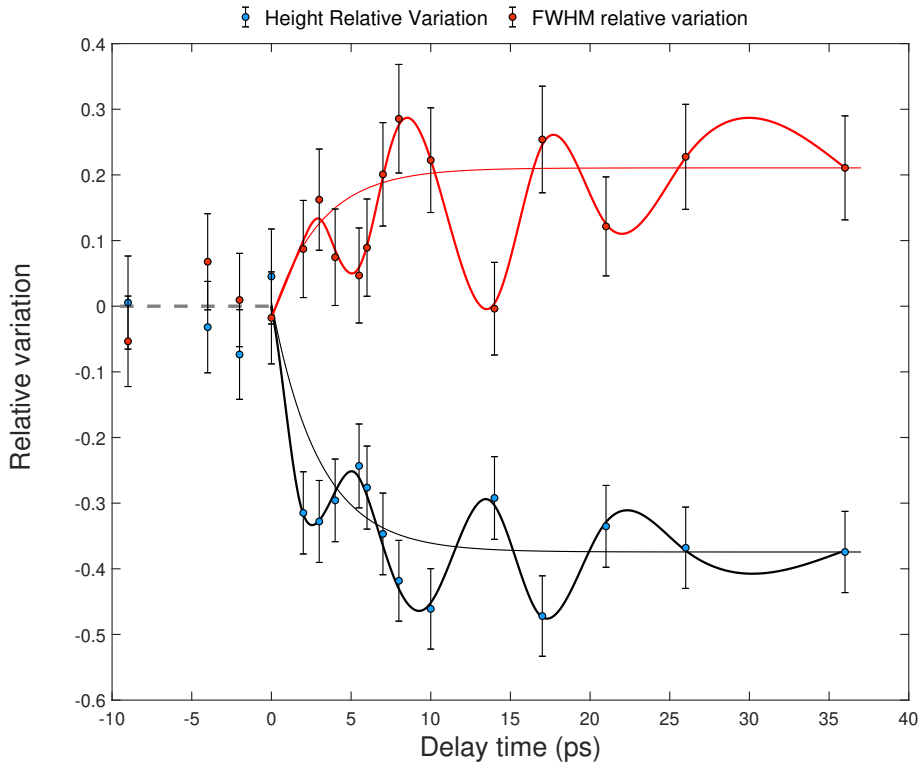

Figure V.12: Peak height and peak width relative variations for the monocrystalline gold sample.

A different data analysis was carried out for the polycrystalline gold sample. We acquired several diffraction images with different delay line position. Even in this case, for each acquisition, we first performed ultrafast electron diffraction without the pump ("preshot"), and then we did the pump – probe ("pumped"). Differently with respect to the diamond case, we could acquire 20 images per delay. For each delay time, I did the average of all the preshot and pumped images (Figure V.9). Then, I performed a radial integral of the average images, calculating the barycentre of the direct beam and setting it as centre. In Figure V.13 a typical plot of the intensity in function of the distance is shown. Before fitting the integrated curve, I decided to apply a Savitzky – Golay filter to smooth the data. This approach allows the fitting curve to adapt better to the experimental data. I also estimated the baseline to subtract to the integrated curve to be a parabolic curve (red line in Figure V.13 (left)). The fitting function, red line in Figure V.13 (right), is the sum of five gaussians

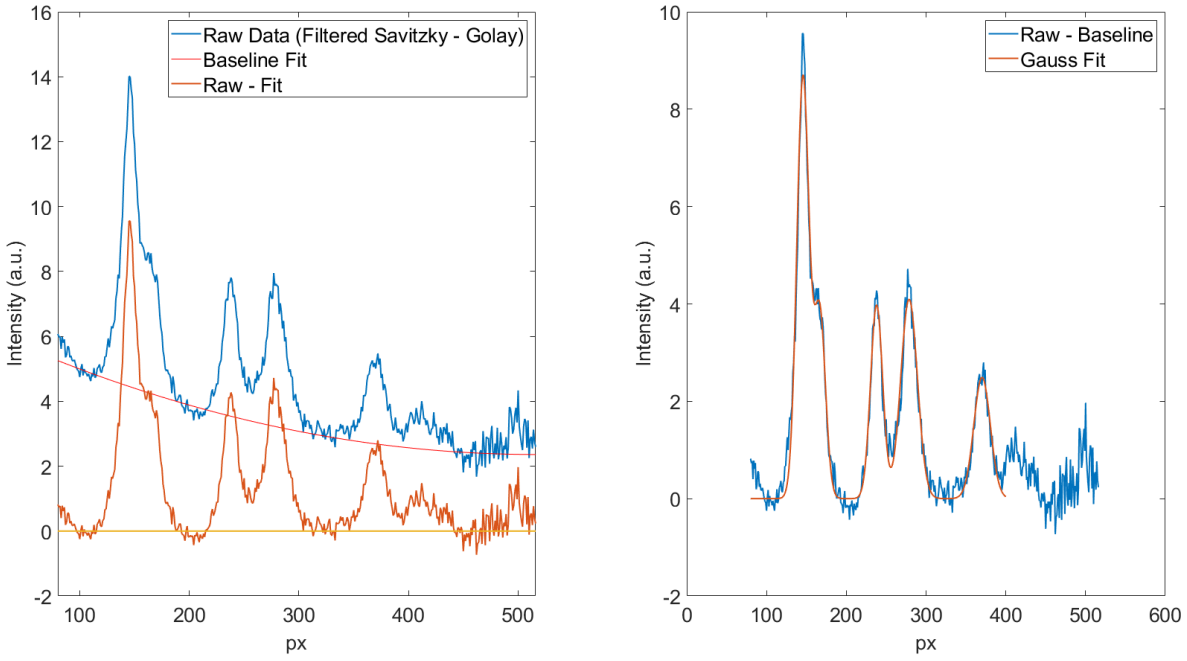

Figure V.13: (left) Intensity radial distribution for polycrystalline gold (blue line). The orange curve was obtained by subtracting the baseline (red curve) from the initial data. (right) Gaussian fit of the experimental data.

Initially, I fit the data using the Pseudo – Voigt function (Equation (V.1)). However, the value of the linear coefficient η varied of 1% with respect to $\eta = 1$, which is the limiting case in which the Pseudo Voigt becomes a gaussian. I preferred to use one fitting parameter less, using the gaussian. Note that we didn't have the energy resolution of the detector to resolve the peaks (111) from (200) and (220-311-222). We decided to

consider only the peak (400). Figure V.14 shows, as expected, a plateau for $t < 0$ and an exponential behaviour for positive times. Simultaneously, while the peak drop decreases, the width increases. Even in this case, the lattice melting process occurs in about 1 ps.

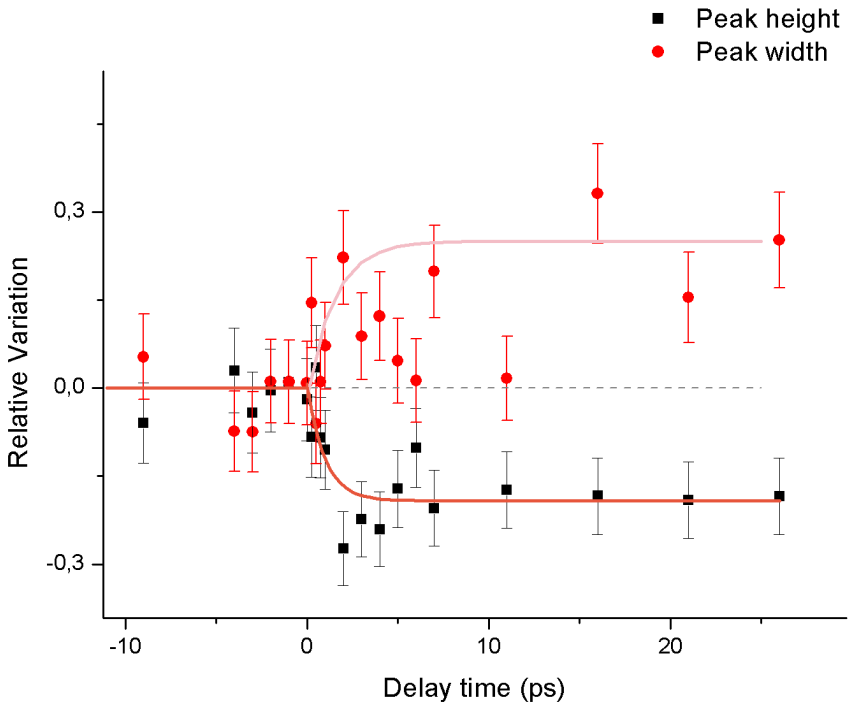

Figure V.14: Peak height and peak width relative variation for the polycrystalline gold sample.

Chapter VI

Conclusions

One of the most exciting opportunities opened by FELs is the feasibility of performing, for the first time, pump-probe experiments in the Extreme Ultraviolet (EUV) and X-ray wavelength regimes with femtosecond time resolution or even below. In the pump-probe scheme, a first light pulse (IR, Vis, EUV, EUV or X-ray) initiates dynamics, like a chemical reaction, a phase transition, spin-, orbital, or charge-density waves in solids and a second pulse, impinging at well-defined time delay, probes the sample. In this work, we presented a pioneering setup that allows the investigation of ultrafast dynamics involving the atomic structure. We succeeded in combining a sub-relativistic compressed electron probe with the seeded Free Electron Laser (FEL) pump at the FERMI facility. The time jitter between pump and probe was smaller than 10 fs. This fact guarantees the time resolution necessary to investigate sub-ps dynamics. We tested our setup on polycrystalline gold, diamond single crystal, and gold single crystal. Our UED measurements indicate that the melting process in FEL-excited materials occurs in about 1 ps. This extremely short time scale suggests the activation of a non-thermal melting mechanism governed by ultrafast changes in the electronic system without assistance from the phonon system.

References

[1] A. Zewail, "Femtochemistry: Atomic-scale dynamics of the chemical bond using ultrafast lasers (nobel lecture)," *Angewandte Chemie International Edition*, vol. 39, pp. 2586–2631, Aug. 2000. DOI: 10.1002/1521-3773(20000804)39:15<2586::AID-ANIE2586>3.0.CO;2-O.

[2] J. Als-Nielsen and D. McMorrow, *Elements of Modern X-ray Physics: Als-Nielsen/Elements*. Hoboken, NJ, USA: John Wiley & Sons, Inc., Mar. 2011, ISBN: 9781119998365 9780470973950. DOI: 10.1002/9781119998365. [Online]. Available: http://doi.wiley.com/10.1002/9781119998365 (visited on 09/30/2019).

[3] H. P. Freund and T. M. Antonsen, *Principles of free-electron lasers*, eng, 2. ed. London: Chapman & Hall, 1996, OCLC: 832754138, ISBN: 9780412725401.

[4] J. C. Sheppard. (2002). Helical undulator radiation, [Online]. Available: http://www.phy.princeton.edu/~kirkmcd/e166/LCC%20notes/LCC-0095.pdf (visited on 09/01/2019).

[5] P. Schmüser, M. Dohlus, and J. Roßbach, *Ultraviolet and soft X-ray free electron lasers: introduction to physical principles, experimental results, technological challenges*, eng, ser. Springer tracts in modern physics 229. Berlin: Springer, 2008, OCLC: 263412560, ISBN: 9783540795711 9783540795728.

[6] Elettra-Sincrotrone Trieste S.C.p.A. (2018). Diagnostica e Linee di luce, [Online]. Available: https://www.elettra.trieste.it/it/lightsources/fermi/diagnostica-e-linee-di-luce.html (visited on 09/01/2019).

[7] Ayvazyan, V. Baboi, N. Bohnet, I. Brinkmann, R. Castellano, M. Castro, P. Catani, L. Choroba, S. Cianchi, A. Dohlus, M. Edwards, H. T. Faatz, B. Fateev, A. A. Feldhaus, J. Flöttmann, K. Gamp, A. Garvey, T. Genz, H. Gerth, Ch. Gretchko, V. Grigoryan, B. Hahn, U. Hessler, C. Honkavaara, K. Hüning, M. Ischebeck, R. Jablonka, M. Kamps, T. Körfer, M. Krassilnikov, M. Krzywinski, J. Liepe, M. Liero, A. Limberg, T. Loos, H. Luong, M. Magne, C. Menzel, J. Michelato, P. Minty, M. Müller, U.-C. Nölle, D. Novokhatski, A. Pagani, C. Peters, F. Pflüger, J. Piot, P.

Plucinski, L. Rehlich, K. Reyzl, I. Richter, A. Rossbach, J. Saldin, E. L. Sandner, W. Schlarb, H. Schmidt, G. Schmüser, P. Schneider, J. R. Schneidmiller, E. A. Schreiber, H.-J. Schreiber, S. Sertore, D. Setzer, S. Simrock, S. Sobierajski, R. Sonntag, B. Steeg, B. Stephan, F. Sytchev, K. P. Tiedtke, K. Tonutti, M. Treusch, R. Trines, D. Türke, D. Verzilov, V. Wanzenberg, R. Weiland, T. Weise, H. Wendt, M. Will, I. Wolff, S. Wittenburg, K. Yurkov, M. V. Zapfe, K., "Generation of gw radiation pulses from a vuv free-electron laser operating in the femtosecond regime," *Physical Review Letters*, vol. 88, p. 104 802, 10 2002, ISSN: 0031-9007,1079-7114. DOI: 10.1103/physrevlett.88.104802. [Online]. Available: http://doi.org/10.1103/physrevlett.88.104802.

[8] C. Bocchetta, A. Abrami, E. Allaria, I. Andrian, D. Bacescu, L. Badano, L. Banchi, D. Bulfone, C. Bontoiu, R. Bracco, F. Cargnello, K. Casarin, M. Cornacchia, P. Craievich, D. Cocco, M. Danailov, G. D'Auria, A. Demidovich, G. Ninno, and D. Zangrando, *FERMI@Elettra Conceptual Design Report*. Jan. 2007.

[9] Elettra-Sincrotrone Trieste S.C.p.A. (2018). FERMI machine description. Main machine characteristics, [Online]. Available: https://www.elettra.trieste.it/it/lightsources/fermi/fermi-machine/fermi-description.html (visited on 09/02/2019).

[10] ——, (2018). FERMI machine description. The Photo-injector, [Online]. Available: https://www.elettra.trieste.it/it/lightsources/fermi/fermi-machine/fermi-description/page-2.html (visited on 09/02/2019).

[11] ——, (2018). FERMI machine description. LINAC: Acceleration, Compression and Transport to the Undulators, [Online]. Available: https://www.elettra.trieste.it/it/lightsources/fermi/fermi-machine/fermi-description/page-3.html (visited on 09/02/2019).

[12] Zangrando, M. Abrami, A. Bacescu, D. Cudin, I. Fava, C. Frassetto, F. Galimberti, A. Godnig, R. Giuressi, D. Poletto, L. Rumiz, L. Sergo, R. Svetina, C. Cocco, D., "The photon analysis, delivery, and reduction system at the fermi@elettra free electron laser user facility," *Review of Scientific Instruments*, vol. 80, p. 113 110, 11 2009, ISSN: 0034-6748,1089-7623. DOI: 10.1063/1.3262502. [Online]. Available: http://doi.org/10.1063/1.3262502.

[13] N. N. P. (Mihai Stafe Aurelian Marcu, *Pulsed Laser Ablation of Solids: Basics, Theory and Applications*, 1st ed., ser. Springer Series in Surface Sciences 53. Springer-Verlag Berlin Heidelberg, 2014, ISBN: 978-3-642-40977-6,978-3-642-40978-3.

[14] V. Aslanyan, "Extreme ultraviolet lasers and their interactions with matter," PhD's Thesis, University of York, York, 2016.

[15] N. D. M. Neil W.(Neil W. Ashcroft) Ashcroft, *Solid state physics*, 1st ed., ser. Solid State Physics. Holt, Rinehart and Winston, 1976, ISBN: 0030839939,9780030839931.

[16] C. Kittel, *Introduction to solid state physics*, 7th ed. Wiley, 1996, ISBN: 9780471111818,047111181

[17] B. Rethfeld, A. Kaiser, and M. Vicanek, "Ultrafast dynamics of nonequilibrium electrons in metals under femtosecond laser irradiation," *Physical Review B, v.65 (2002)*, vol. 65, May 2002. DOI: 10.1103/PhysRevB.65.214303.

[18] L. Jiang and H. Tsai, "Improved two-temperature model and its application in ultrashort laser heating of metal films," *Journal of Heat Transfer*, vol. 127, p. 1167, Oct. 2005. DOI: 10.1115/1.2035113.

[19] F. Herman, R. Kortum, and C. Kuglin, "Energy band structure of diamond, cubic silicon carbide, silicon, and germanium," *International Journal of Quantum Chemistry*, vol. 1, pp. 533–566, Jan. 2009. DOI: 10.1002/qua.560010658.

[20] R. Mildren, "Intrinsic optical properties of diamond," in. Mar. 2013, pp. 1–34, ISBN: 9783527411023. DOI: 10.1002/9783527648603.ch1.

[21] M. Mo, Z. Chen, R. Li, M. Dunning, B. B. L. Witte, J. Baldwin, L. Fletcher, J.-B. Kim, A. Ng, R. Redmer, A. Reid, P. Shekhar, X. Shen, M. Shen, K. Sokolowski-Tinten, Y. Tsui, Y. Wang, Q. Zheng, X. Wang, and S. Glenzer, "Heterogeneous to homogeneous melting transition visualized with ultrafast electron diffraction," *Science*, vol. 360, pp. 1451–1455, Jun. 2018. DOI: 10.1126/science.aar2058.

[22] T. van Oudheusden, "Electron source for sub-relativistic single-shot femtosecond diffraction," PhD's Thesis, University of Eindhoven, Eindhoven, 2010.

[23] P. Pasmans, "Ultrafast electron diffraction: An investigation of fundamental limits," PhD's Thesis, University of Eindhoven, Eindhoven, 2014.

[24] P. J. M. H. (Professor Brent Fultz, *Transmission Electron Microscopy and Diffractometry of Materials*. Springer Berlin Heidelberg, 2002, ISBN: 978-3-662-04903-7,978-3-662-04901-3.

[25] G. D.J., *Introduction to quantum mechanics*, 2nd ed. Pearson, 2005.

[26] F. Carbone, P. Musumeci, J. Luiten, and C. Hébert, "A perspective on novel sources of ultrashort electron and x-ray pulses," *Chemical Physics - CHEM PHYS*, vol. 392, Jan. 2012. DOI: 10.1016/j.chemphys.2011.10.010.

[27] J. D. Geiser and P. M. Weber, "High-repetition-rate time-resolved gas phase electron diffraction," in *Time-Resolved Electron and X-Ray Diffraction*, P. M. Rentzepis, Ed., International Society for Optics and Photonics, vol. 2521, SPIE, 1995, pp. 136–144. DOI: 10.1117/12.218345. [Online]. Available: https://doi.org/10.1117/12.218345.

[28] E. Fill, L. Veisz, A. Apolonski, and F. Krausz, "Sub-fs electron pulses for ultrafast electron diffraction," *New Journal of Physics*, vol. 8, no. 11, pp. 272–272, Nov. 2006. DOI: 10.1088/1367-2630/8/11/272. [Online]. Available: https://doi.org/10.1088%2F1367-2630%2F8%2F11%2F272.

[29] T. Oudheusden, E. Jong, B. Siwick, B. van der Geer, W. Root, and J. Luiten, "Electron source concept for single-shot sub-100 fs electron diffraction in the 100 kev range," *Journal of Applied Physics*, vol. 102, Feb. 2007. DOI: 10.1063/1.2801027.

[30] P. Pasmans, G. Ham, S. Dal Conte, B. van der Geer, and J. Luiten, "Microwave tm010 cavities as versatile 4d electron optical elements," *Ultramicroscopy*, vol. 127, Jul. 2012. DOI: 10.1016/j.ultramic.2012.07.011.

[31] J. Franssen and J. Luiten, "Improving temporal resolution of ultrafast electron diffraction by eliminating arrival time jitter induced by radiofrequency bunch compression cavities," *Structural Dynamics*, vol. 4, Mar. 2017. DOI: 10.1063/1.4984104.

[32] A. S. Instrument, *TimePix QTPX-262k and STPX-65k, Quick start user manual.*

[33] T. Oudheusden, P. Pasmans, B. van der Geer, M. De Loos, M. Wiel, and J. Luiten, "Compression of subrelativistic space-charge-dominated electron bunches for single-shot femtosecond electron diffraction," *Physical review letters*, vol. 105, p. 264 801, Dec. 2010. DOI: 10.1103/PHYSREVLETT.105.264801.

[34] V. Levitin, *Interatomic Bonding in Solids: Fundamentals, Simulation, Applications*, 1st ed. Wiley-VCH, 2014, ISBN: 3527335072,9783527335077.

[35] F. Sánchez-Bajo, A. Ortiz, and F. Cumbrera, "Analytical formulation of the variance method of line-broadening analysis for voigtian x-ray diffraction peaks," *J. Appl. Cryst*, vol. 39, pp. 598–600, Aug. 2006. DOI: 10.1107/S0021889806017122.

[36] S. Nie, X. Wang, H. Park, R. Clinite, and J. Cao, "Measurement of the electronic grüneisen constant using femtosecond electron diffraction," *Physical review letters*, vol. 96, p. 025 901, Feb. 2006. DOI: 10.1103/PhysRevLett.96.025901.

[37] D. Fritz, D. Reis, B. Adams, R. Akre, J. Arthur, C. Blome, P. Bucksbaum, A. Cavalieri, S. Engemann, S. Fahy, R. Falcone, P. Fuoss, K. Gaffney, M. George, J. Hajdu, M. Hertlein, P. Hillyard, M. Horn-von Hoegen, M. Kammler, and J. Hastings, "Ultrafast bond softening in bismuth: Mapping a solid's interatomic potential with x-rays," *Science (New York, N.Y.)*, vol. 315, pp. 633–6, Mar. 2007. DOI: 10.1126/science.1135009.

Supplementary Information

1 List of Figures

2 List of Tables